EFFICIENT COMPUTATION OF SURFACE FIELDS EXCITED ON AN ELECTRICALLY LARGE CIRCULAR CYLINDER WITH AN IMPEDANCE BOUNDARY CONDITION

A THESIS

SUBMITTED TO THE DEPARTMENT OF ELECTRICAL AND ELECTRONICS ENGINEERING

AND THE INSTITUTE OF ENGINEERING AND SCIENCE

OF BILKENT UNIVERSITY

IN PARTIAL FULFILLMENT OF THE REQUIREMENTS

FOR THE DEGREE OF

MASTER OF SCIENCE

By

Burak Alişan

July, 2006

I certify that I have read this thesis and that in my opinion it is fully adequate, in scope and in quality, as a thesis for the degree of Master of Science.

Prof. Dr. Ayhan Altıntaş (Advisor)

I certify that I have read this thesis and that in my opinion it is fully adequate, in scope and in quality, as a thesis for the degree of Master of Science.

Asst. Prof. Dr. Vakur B. Ertürk (Co-advisor)

I certify that I have read this thesis and that in my opinion it is fully adequate, in scope and in quality, as a thesis for the degree of Master of Science.

Prof. Dr. Orhan Arıkan

I certify that I have read this thesis and that in my opinion it is fully adequate, in scope and in quality, as a thesis for the degree of Master of Science.

Prof. Dr. Gülbin Dural

I certify that I have read this thesis and that in my opinion it is fully adequate, in scope and in quality, as a thesis for the degree of Master of Science.

Asst. Prof. Dr. Lale Alatan

Approved for the Institute of Engineering and Science:

Prof. Dr. Mehmet Baray
Director of the Institute

ABSTRACT

EFFICIENT COMPUTATION OF SURFACE FIELDS EXCITED ON AN ELECTRICALLY LARGE CIRCULAR CYLINDER WITH AN IMPEDANCE BOUNDARY CONDITION

Burak Alişan
M.S. in Electrical and Electronics Engineering
Supervisor: Prof. Dr. Ayhan Altıntaş
July, 2006

An efficient computation technique is developed for the surface fields excited on an electrically large circular cylinder with an impedance boundary condition (IBC). The study of these surface fields is of practical interest due to its applications in the design and analysis of conformal antennas. Furthermore, it acts as a canonical problem useful toward the development of asymptotic solutions valid for arbitrary smooth convex thin material coated/partially material coated surfaces.

In this thesis, an alternative numerical approach is presented for the evaluation of the Fock type integrals which exist in the Uniform Geometrical Theory of Diffraction (UTD) based asymptotic solution for the non-paraxial surface fields excited by a magnetic or an electric source located on the surface of an electrically large circular cylinder with an IBC. This alternative approach is based on performing a numerical integration of the Fock type integrals on a deformed path on which the integrands are non-oscillatory and rapidly decaying. Comparison of this approach with the previously developed study presented by Tokgöz (PhD thesis, 2002), which is based on invoking the Cauchy's residue theorem by finding the pole singularities numerically, reveals that the alternative approach is considerably more efficient. Since paraxial solution is a closed-form solution and very efficient in terms of computational time, there is no need for an alternative approach for the evaluation of the paraxial surface fields.

Keywords: Surface fields, Impedance cylinder, UTD based Green's functions, Fock type integrals.

ÖZET

EMPEDANS SINIR KOŞULLARI OLAN ELEKTRİKSEL OLARAK BÜYÜK BİR ÇEMBERSEL SİLİNDİR ÜZERİNDEKİ YÜZEY DALGALARININ VERİMLİ ŞEKİLDE HESAPLANMASI

Burak Alişan
Elektrik ve Elektronik Mühendisliği, Yüksek Lisans
Tez Yöneticisi: Ayhan Altıntaş
Temmuz, 2006

Empedans sınır koşulları olan elektriksel olarak büyük bir çembersel silindir üzerinde oluşturulan yüzey dalgaları için verimli bir hesaplama tekniği geliştirilmiştir. Bu yüzey dalgaları üzerinde yapılan çalşma konformal antenlerin tasarım ve analiz uygulamalarından dolayı önemlidir. Ayrıca, tamamen veya kısmen ince materyal kaplı dışbükey yüzeyler için geçerli asimptotik çözümlerin geliştirilmesinde yararlı olacak kanonik bir problem gibi davranır.

Bu tezde, empedans sınır koşulları olan elektriksel olarak büyük bir çembersel silindir üzerine yerleştirilmiş bir manyetik veya elektrik kaynağı tarafından oluşturulan eksensel olmayan yüzey dalgaları için geçerli olan UTD'ye dayalı asimptotik çözümlerde bulunan Fock tipi integrallerin hesaplanması için alternatif bir sayısal yaklaşım sunulmuştur. Bu alternatif yaklaşım, Fock tipi integrallerin salınımsız olduğu ve hızla azaldığı biçimi bozulmuş bir yol üzerindeki sayısal integrasyonununa dayandırılmıştır. Bu yaklaşımın daha önce Tokgöz (Doktora tezi, 2002) tarafından geliştirilmiş kutup tekilliklerinin sayısal olarak bulunarak Cauchy residue teoreminin uygulanmasına dayandırılmış yaklaşımla karşılaştırılması alternatif yaklaşımın çok daha verimli olduğunu ortaya çıkarmıştır. Eksensel çözümün bir kapalı form çözüm olması ve hesaplama zamanı bakımından çok verimli olmasından dolayı, eksensel yüzey dalgalarının hesaplanmasında bir alternatif yaklaşıma ihtiyaç yoktur.

Anahtar sözcükler: Yüzey dalgaları, Empedans silindiri, UTD'ye dayalı Green fonksiyonu, Fock tipi integraller.

To My Family

Acknowledgement

I would like to express my gratitude to my advisors Prof. Dr. Ayhan Altıntaş and Asst. Prof. Dr. Vakur B. Ertürk for their instructive comments and continuing support in the supervision of the thesis.

I would like to express my special thanks and gratitude to Prof. Dr. Orhan Arıkan, Prof. Dr. Gülbin Dural and Asst. Prof. Dr. Lale Alatan for showing keen interest to the subject matter and accepting to read and review the thesis.

Finally I would like to thank Aselsan Inc. for letting me to involve in this thesis study and my family for their support.

Contents

List of Figures

Chapter 1

Introduction

Many military and commercial applications (e.g., missiles, mobile base stations, transreceivers of Multi Input Multi Output (MIMO) systems which might be mounted on curved host platforms, etc.) have stringent aerodynamic constraints that require the use of antennas that conform to their host platforms. This necessitates the development of efficient and accurate design and analysis tools for this class of antennas. Therefore, surface fields, created by a current distribution on the surface of a thin material coated (lossy or lossless) perfect electric conducting (PEC) circular cylinder, have been studied extensively using an impedance boundary condition (IBC). Analysis of slot/aperture antennas as well as antennas on partially coated host platforms are typical applications which require the fast and accurate evaluation of these surface fields. Furthermore, the study of these surface fields acts as a canonical problem useful toward the development of asymptotic solutions valid for arbitrary smooth convex thin material coated/partially material coated surfaces [1], [2].

High frequency based asymptotic solutions for the surface fields on a source excited PEC convex surface have been investigated previously. Approximate expressions were obtained for the magnetic field induced by slots on electrically large conducting circular cylinder [3]. Later, improved Geometrical Theory of Diffraction (GTD) and Uniform Geometrical Theory of Diffraction (UTD) based representations were presented for the surface fields due to a slot on a PEC cylinder [4]. A simple approximate expression for the surface magnetic field due to a magnetic dipole on a conducting circular cylinder was developed in [5]. The surface field solution obtained in [5] contains an additional term taken from [6] because of the need to obtain an accurate solution in the paraxial (nearly axial) region of the cylinder. Furthermore, an approximate asymptotic solution was presented for the electromagnetic fields which are induced on an electrically large perfectly conducting smooth convex surface by an infinitesimal magnetic or electric current moment on the same surface [7]. In [8], the accuracy of the existing approximate asymptotic solutions for the surface field due to a magnetic dipole on a large conducting cylinder was tested by comparing them with the exact modal solution. Based on this comparison, a new approximate solution with improved accuracy for the surface field due to a magnetic point source on a cylinder was presented in [9].

However, the study of surface fields created by a current distribution on the surface of an impedance circular cylinder, which can also model a thin (lossy/lossless) material coated PEC case [10], is still a challenging problem. Recently, several high frequency based asymptotic solutions for the surface fields on a source excited circular cylinder with an IBC have been presented valid away from the paraxial region, and within the paraxial region. High frequency based solution for a surface field excited by a magnetic line source on an impedance cylinder has been presented in [11]. Later, a high frequency asymptotic solution has been introduced for the vector potentials for a point source on an anisotropic impedance cylinder [12]. In [13], an approximate asymptotic solution based on the Uniform Geometrical Theory of Diffraction (UTD) has been proposed for the magnetic fields excited at a point by an infinitesimal magnetic current moment located at another point, both on the surface of an electrically large circular cylinder with a finite surface impedance. Afterwards, approximate solutions have been developed for the surface magnetic field on a magnetic current excited circular cylinder with an IBC in [14]. Recently, an alternative approximate asymptotic closed-form solution has been proposed for the accurate representation of the tangential surface magnetic field within the paraxial region of a tangential magnetic current excited circular cylinder with an IBC in [15].

Among these aforementioned works related to impedance circular cylinders, the UTD based asymptotic solution for a three dimensional geometry (circular cylinder with an IBC) [12]-[14] (valid away from the paraxial region) involves some Fock type integrals and their derivatives which have to be evaluated numerically. However, special care is required in the computation of these integrals since the efficiency and accuracy of the overall solution strongly depends on the numerical evaluation of these integrals. In [14] (and in [12]-[13]), these Fock type integrals have been evaluated by invoking the Cauchy's residue theorem, which requires finding the corresponding pole singularities numerically. It is claimed that the residue contributions coming from the first 20 poles yield sufficient accuracy.

Keeping this issue in mind, in this thesis, an alternative numerical approach is proposed for the evaluation of the Fock type integrals (and their derivatives) which is based on performing a numerical integration along a deformed path. On this path, the Fock type integrals exhibit a non oscillatory and rapidly decaying nature. Hence, using a simple Gaussian quadrature algorithm is enough to obtain very accurate results efficiently. Consequently, this alternative approach is easier to implement and requires less computational time compared to the approach presented in [14]. It should be noted that, the concept of performing a numerical integration on similar deformed integration paths has been previously used for the evaluation of surface fields of source excited electrically large dielectric coated circular cylinders in [16]-[19], and accurate results have been obtained. Moreover, the UTD based surface fields due to a tangential electric current source, which are valid away from the paraxial region, are also derived using an IBC, and evaluated both performing an integration along the aforementioned deformed path and invoking the Cauchy's residue theorem (similar to [14]), whereas in [14] only the magnetic source case was considered.

Besides, the approximate closed-form solution given for the tangential surface magnetic field within the paraxial region of a tangential magnetic current excited circular cylinder with an IBC in [14] and [15] is briefly reviewed. In this solution, Green's function representations are written in terms of spectral double integrals involving Hankel function. The integrals are evaluated approximately using the large argument representation of the Hankel function. Since it is a closed-form solution, it is very efficient in terms of the computational time. Thus, UTD based solution (valid in the non-paraxial region), evaluated with numerical integration approach, and closed-form paraxial solution form a complete and efficient solution for the Green's function representations pertaining the surface magnetic field on an electrically large circular cylinder with an IBC.

The organization of this thesis is as follows: In Section II, the UTD based asymptotic solutions for the surface fields excited by both a magnetic and an electric line source (2-D case), as well as both a magnetic and an electric point source (3-D case) located on the surface of an electrically large impedance cylinder are given. The numerical evaluation of these surface fields are discussed in Section III, which presents a review of the approach presented in [14], and a detailed description of the alternative approach, namely the numerical integration along a deformed integration path, and closed-form solution given for surface fields in paraxial region. In Section IV, several numerical results for the surface fields for both 2-D and 3-D cases are obtained using the two aforementioned approaches. An e^{jwt} time dependence is assumed and suppressed throughout this thesis.

Chapter 2

An Asymptotic Solution for the Surface Fields Excited on a Circular Cylinder with an IBC

2.1 Two-Dimensional Case

In this section, an asymptotic solution for the magnetic field due to a magnetic line source excitation, given in [11], is briefly reviewed, and an asymptotic solution for the electric field due to an electric source excitation is introduced. Consider a circular cylinder with an IBC as shown in Fig. 2.1. The cylinder has a radius a, a uniform surface impedance Z_s, and is oriented along the z axis.

2.1.1 Solution to the TE_z Problem

An asymptotic solution for the magnetic field excited by a magnetic line source $\vec{M} = \hat{z}M_0$ is presented. Magnetic field excited by $\vec{M}$ has only a $\hat{z}$ component, and satisfies the inhomogeneous scalar wave equation

$$(\nabla^2 + k^2)H_z = \frac{jk}{Z_0}M_0 \tag{2.1}$$

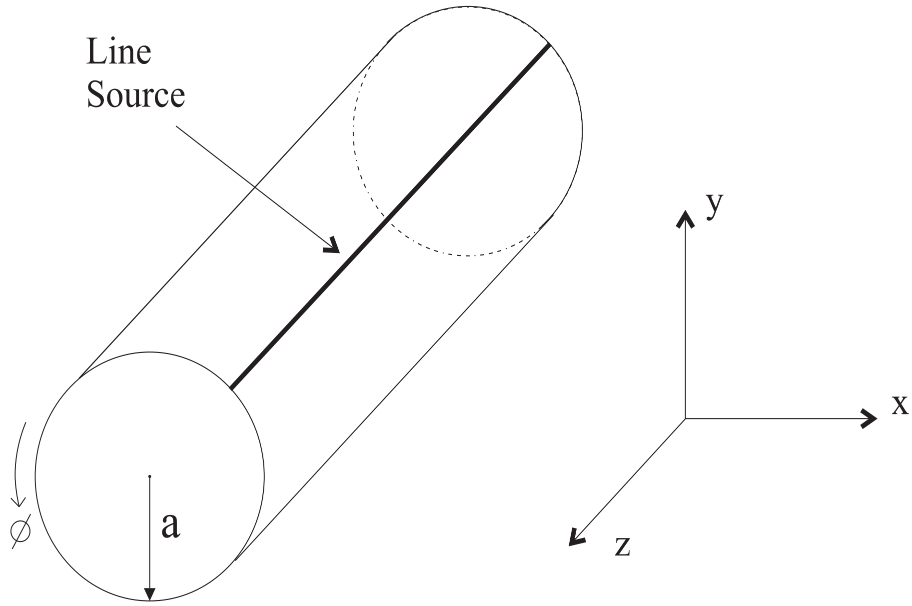

Figure 2.1: Line source on a circular cylinder with a radius a

where k is the free space wave number, and Z_0 is the intrinsic impedance of the free space. The impedance boundary condition at the surface of the cylinder ($\rho = a$) is given as

$$\frac{\partial H_z}{\partial \rho} - jk\Lambda H_z = 0 \tag{2.2}$$

where $\Lambda = Z_s/Z_0$ is the normalized surface impedance. The solution to the surface magnetic field has the form

$$H_z(\rho = a, \phi) = -\frac{jk}{Z_0} G^m \tag{2.3}$$

where G^m is the summation of all ray encirclements, which are propagating in the positive and negative ϕ directions around the cylinder. In [11], for the calculation of G^m only the two dominant surface ray contributions are taken into consideration, and G^m is expressed as

$$G^m \sim \frac{-j}{2} H_0^{(2)}(kt_1)\nu(\xi_1, q) - \frac{j}{2} H_0^{(2)}(kt_2)\nu(\xi_2, q) \tag{2.4}$$

where

$$\xi_{1,2} = m\phi_{1,2}\ ; \quad t_{1,2} = a\phi_{1,2} \tag{2.5}$$

with

$$m = (ka/2)^{1/3}\ ; \quad \phi_1 = \phi\ ; \quad \phi_2 = 2\pi - \phi \tag{2.6}$$

$$q = -jm\Lambda \tag{2.7}$$

and

$$\nu(\xi, q) = \frac{1}{2}e^{j\pi/4}\sqrt{\frac{\xi}{\pi}}\int_{-\infty}^{\infty}\frac{e^{-j\xi\tau}}{R_w - q}d\tau \tag{2.8}$$

with $R_w = W_2'(\tau)/W_2(\tau)$, $W_2(\tau)$ is a Fock-type Airy function, $W_2'(\tau)$ is its derivative with respect to τ.

2.1.2 Solution to the TM_z Problem

An asymptotic solution for the electric field excited by an electric line source $\vec{J} = \hat{z}J_0$ is presented. The electric field excited by $\vec{J}$ has only a $\hat{z}$ component, and satisfies the inhomogeneous scalar wave equation given by

$$(\nabla^2 + k^2)E_z = jkZ_0J_0. \tag{2.9}$$

The impedance boundary condition at the surface of the cylinder ($\rho = a$) is

$$\frac{\partial E_z}{\partial \rho} - jk\Lambda^{-1}E_z = 0 \tag{2.10}$$

where $\Lambda = Z_s/Z_0$ is the normalized surface impedance. The solution to the surface electric field has the form

$$E_z(\rho = a, \phi) = -jkZ_0G^e \tag{2.11}$$

where G^e can be expressed as

$$G^e \sim \frac{-j}{2}H_0^{(2)}(kt_1)\nu(\xi_1, q) - \frac{j}{2}H_0^{(2)}(kt_2)\nu(\xi_2, q) \tag{2.12}$$

in which $q = -jm\Lambda^{-1}$, and Fock type integral $\nu(\xi, q)$ is the same function given by (2.8).

As expected, the $\hat{z}$ component of the electric field, E_z, obtained for the electric line source excitation is the dual of the $\hat{z}$ component of the magnetic field, H_z, obtained for the magnetic line source excitation.

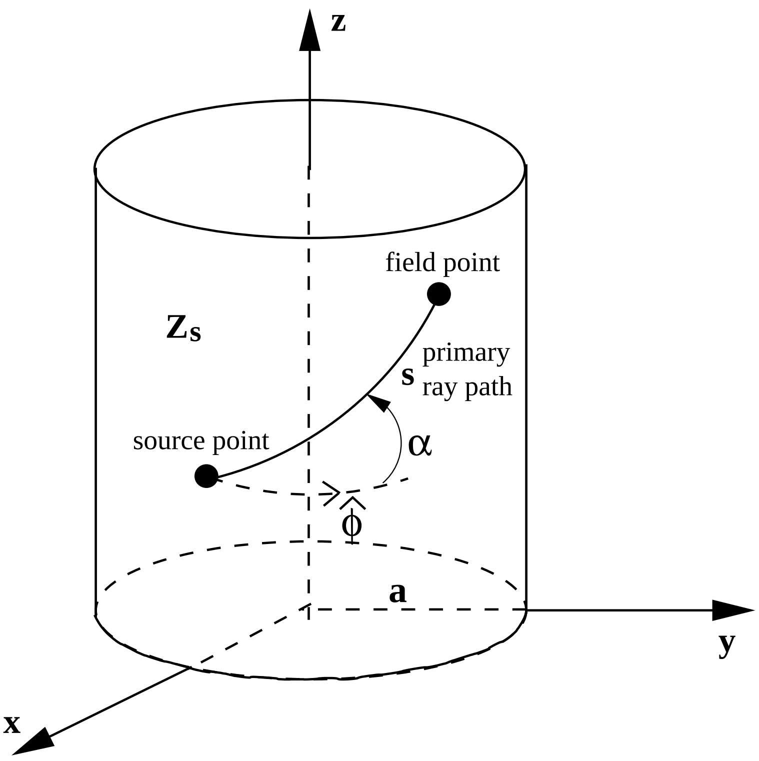

Figure 2.2: Geometry of a circular cylinder with a radius a

2.2 Three-Dimensional Case

Consider an electrically large circular cylinder with an IBC as shown in Fig. 2.2. The cylinder has a radius a, a uniform surface impedance Z_s, and is assumed to be infinitely long along its axial direction.

2.2.1 Solution to the Surface Fields in the Non-paraxial Region (UTD Based Solution)

An asymptotic solution for the surface fields excited by a magnetic or an electric source located on the surface of a circular cylinder is derived using Airy function approximation of Hankel function.

A. Magnetic Source Excitation

For such a cylinder, $\hat{z}$ components of the electric and magnetic fields due to a tangential magnetic source

$$\vec{P}_m = P_m^z \hat{z} + P_m^\phi \hat{\phi} \tag{2.13}$$

located on the surface is expressed in [14] as

$$\begin{aligned} E_z &= \frac{1}{4\pi^2 a}\int_{-\infty}^{\infty} dk_z e^{-jk_z z_d} \sum_{n=-\infty}^{\infty} \frac{e^{jn\phi_d}}{D_c}[\frac{nk_z}{k_\rho^2 a}P_m^z + (1+\frac{j\Lambda^{-1}k}{k_\rho}R_n)P_m^\phi] \\ &\quad \frac{H_n^{(2)}(k_\rho \rho)}{H_n^{(2)}(k_\rho a)} \end{aligned} \tag{2.14}$$

$$\begin{aligned} H_z &= -\frac{1}{4\pi^2 a Z_s}\int_{-\infty}^{\infty} dk_z e^{-jk_z z_d} \sum_{n=-\infty}^{\infty} \frac{e^{jn\phi_d}}{D_c}[(1+\frac{j\Lambda k}{k_\rho}R_n)P_m^z + \frac{nk_z}{k_\rho^2 a}P_m^\phi] \\ &\quad \frac{H_n^{(2)}(k_\rho \rho)}{H_n^{(2)}(k_\rho a)} \end{aligned} \tag{2.15}$$

where

$$R_n = \frac{H_n^{(2)'}(k_\rho a)}{H_n^{(2)}(k_\rho a)} \tag{2.16}$$

$$D_c = (1+\frac{j\Lambda k}{k_\rho}R_n)(1+\frac{j\Lambda^{-1}k}{k_\rho}R_n) - (\frac{nk_z}{k_\rho^2 a})^2 \tag{2.17}$$

and

$$z_d = z - z' \qquad \phi_d = \phi - \phi'. \tag{2.18}$$

Using the $\hat{z}$ components of the fields (E_z, H_z), the vector potentials (A_z, F_z) due to these components are found via the methods described in [20]. Then, the procedure for the development of high frequency solutions, which is explained in [14], is followed. The details of the procedure are given for the electric source excitation in Appendix B. In this procedure, Watson transform, which is expressed in Appendix C, is applied to the potentials and thereby the potentials are expressed as double integrals over axial (k_z) and azimuthal (ν) wavenumbers. After employing a Fock-substitution ($\nu = k_\rho a + m_t \tau$), integration in the ν-plane is replaced by integration in the τ-plane. Then, introducing a standard polar transformation along with some geometrical relations, integration over k_z is converted to a complex contour integral which is evaluated applying the method of steepest descent, which is expressed in Appendix D, assuming that the separation s between the source and field points is the large parameter. Finally, field expressions are obtained by performing the derivatives to the resultant potential expressions analytically (where the terms including higher powers of m_t^{-2} are neglected). As a result, the tangential surface field excited by a tangential magnetic source given by (2.13) is expressed in [14] as

$$\vec{H}_t = \vec{P}_m \cdot (\hat{z}'\hat{z}G^m_{zz} + \hat{\phi}'\hat{z}G^m_{z\phi} + \hat{z}'\hat{\phi}G^m_{\phi z} + \hat{\phi}'\hat{\phi}G^m_{\phi\phi}) \tag{2.19}$$

where $\vec{P}_m$ represents the strength and the orientation of the magnetic current and G^m_{pq} is a UTD based Green's function representation for a $\hat{p}$ ($\hat{p} = \hat{z}$ or $\hat{\phi}$) oriented surface magnetic field due to a $\hat{q}$ ($\hat{q} = \hat{z}$ or $\hat{\phi}$) directed magnetic current. Note that by relating the magnetic current to the magnetic field as in (2.19), the Green's function representation G^m_{pq} is defined to have a unit of $1/(m^2\,\Omega)$. In (2.19), G^m_{pq} represents the summation of all ray encirclements around the cylinder and can be determined as

$$G^m_{pq} = \sum_{\ell=0}^{\infty}(G^{m_{\ell}+}_{pq} + G^{m_{\ell}-}_{pq}) \tag{2.20}$$

where $G^{m_{\ell}+}_{pq}$ pertains to the Green's function which is responsible from the surface waves propagating around the cylinder in the positive $\hat{\phi}$ direction, whereas $G^{m_{\ell}-}_{pq}$ corresponds to those propagating in the negative $\hat{\phi}$ direction. Provided that the cylinder is electrically large (more than a free-space wavelength in radius), it is enough to retain the $\ell = 0$ term ([14]), which corresponds to the primary rays propagating around the cylinder. Consequently, the UTD based asymptotic Green's function representations for various source and field orientations are given in [14] as

$$\begin{aligned} G^{m\pm}_{zz} \;&\sim\; G_0\{\cos^2\alpha V_0 + \frac{j}{ks}(1-\frac{j}{ks})(2-3\cos^2\alpha)V_0 + [\frac{j}{3ks}(1-\frac{j}{ks}) \\ &\quad \sin^2\alpha - \frac{\cos 2\alpha}{36k^2s^2}]V_1 + \frac{\sin^2\alpha}{36k^2s^2}V_2\} \end{aligned} \tag{2.21}$$

$$\begin{aligned} G^{m\pm}_{z\phi} \;&\sim\; \mp G_0\{\cos\alpha\sin\alpha[1-\frac{j3}{ks}(1-\frac{j}{ks})]Y_0 + [\frac{j}{3ks}(\tan^2\alpha + \frac{j}{ks}) \\ &\quad \cos\alpha\sin\alpha - \frac{\tan\alpha\cos 2\alpha}{6k^2s^2}]Y_1 + \frac{\tan\alpha\sin^2\alpha}{36k^2s^2}Y_2\} \end{aligned} \tag{2.22}$$

$$
\begin{aligned}
G^{m\pm}_{\phi z} \;\; &\sim \;\; \mp G_0\{\cos\alpha\sin\alpha[X_0 + V_0 - \frac{j3}{ks}(1-\frac{j}{ks})V_0] + [\frac{j}{k}(1-\frac{j}{ks})(\frac{2\tan\alpha}{3s} \\
&\quad -\frac{\cos\alpha\sin\alpha}{3s}) - \frac{\sin 2\alpha}{6k^2s^2}]V_1 - \frac{\sin\alpha}{36s^2}(\cos\alpha - \frac{4}{\cos\alpha})V_2\} \qquad (2.23) \\
G^{m\pm}_{\phi\phi} \;\; &\sim \;\; G_0\{\sin^2\alpha Y_0 + \frac{j}{ks}(1-\frac{j}{ks})(2-3\sin^2\alpha)Y_0 + \frac{j}{ks}\frac{1}{\cos^2\alpha}(U_0 - Y_0) \\
&\quad +[\frac{j}{ks}(1-\frac{j}{ks})(\frac{\cos^2\alpha - \sin^2\alpha - 4}{6s}) - \frac{j}{6s}(\cos\alpha - \frac{4}{\cos\alpha} \\
&\quad -\frac{j}{ks}\tan\alpha\sin\alpha) - \frac{\tan\alpha\sin 2\alpha}{6k^2s^2}]Y_1 - (\frac{\sin^2\alpha + 4\tan^2\alpha}{36k^2s^2})Y_2\} \qquad (2.24)
\end{aligned}
$$

where $G_0 = -\frac{jke^{-jks}}{2\pi Z_0 s}$, k is the free space wave number, Z_0 is the free space impedance, s is the geodesic ray path, and α is the angle between s and the positive $\hat{\phi}$ direction as shown in Fig. 2.2. It should be mentioned that the expressions given in (2.21)-(2.24) are valid in the non-paraxial region, and developed mainly for large separations, s, between the source and field points. However, since some of the second order terms in s are included, they may remain accurate even for relatively small separations.

The U_0, X_0, V_0, Y_0, V_1, Y_1, V_2, and Y_2 terms in the above equations ((2.21)-(2.24)) are expressed in [14] in terms of simpler Fock type integrals in the form of

$$\Upsilon_r = \int_{-\infty}^{\infty} d\tau e^{-j\xi\tau}\frac{(R_w)^r}{D_w} \quad ; \qquad r = 0, 1, 2 \tag{2.25}$$

where

$$D_w = (R_w - q_e)(R_w - q_m) + q_c^2 \tag{2.26}$$

$$q_e = -jm_t\Lambda\cos\alpha \tag{2.27}$$

$$q_m = -jm_t\Lambda^{-1}\cos\alpha \tag{2.28}$$

$$q_c = -jm_t(1 + \frac{\tau}{2m_t^2})\sin\alpha \tag{2.29}$$

$$R_w = W_2'(\tau)/W_2(\tau) \tag{2.30}$$

in which $W_2(\tau)$ is a Fock-type Airy function, $W_2'(\tau)$ is its derivative with respect to τ. Besides, $\Lambda = Z_s/Z_0$ is the normalized surface impedance (similar to the 2-D case), the Fock parameter

$$\xi = m_t\phi_\ell^{\pm} \tag{2.31}$$

with

$$m_t = (\frac{k_\rho a}{2})^{1/3}\,; \quad \phi_\ell^\pm = \pm(\phi - \phi' - \pi) + (2\ell + 1)\pi, \tag{2.32}$$

k_z and k_ρ are the axial and radial wave numbers, respectively such that

$$k_\rho = \begin{cases} \sqrt{k^2 - k_z^2} & \text{if } k^2 \geq k_z^2 \\ -j\sqrt{k_z^2 - k^2} & \text{if } k^2 < k_z^2. \end{cases} \tag{2.33}$$

The simplified equations are, in turn, given in [14] as follows:

$$U_0 = -j\xi q_m \sqrt{\frac{j\xi}{\pi}}(\Upsilon_2 - q_e \Upsilon_1) \tag{2.34}$$

$$X_0 = -\frac{1}{2}\sqrt{\frac{j\xi}{\pi}}(\Upsilon_1 + \frac{j}{2m_t^2}\frac{\partial \Upsilon_1}{\partial \xi}) \tag{2.35}$$

$$V_0 = \frac{1}{2}\sqrt{\frac{j\xi}{\pi}}(\Upsilon_1 - q_m \Upsilon_0) \tag{2.36}$$

$$Y_0 = -\frac{q_m}{2}\sqrt{\frac{j\xi}{\pi}}(\Upsilon_0 + \frac{j}{2m_t^2}\frac{\partial \Upsilon_0}{\partial \xi}) \tag{2.37}$$

$$V_1 = \frac{1}{2}\sqrt{\frac{j\xi}{\pi}}[\Upsilon_1 - q_m \Upsilon_0 + 2\xi(\frac{\partial \Upsilon_1}{\partial \xi} - q_m \frac{\partial \Upsilon_0}{\partial \xi})] \tag{2.38}$$

$$Y_1 = -\frac{q_m}{2}\sqrt{\frac{j\xi}{\pi}}[\Upsilon_0 + (\frac{j}{2m_t^2} + 2\xi)\frac{\partial \Upsilon_0}{\partial \xi}] \tag{2.39}$$

$$V_2 = \frac{1}{2}\sqrt{\frac{j\xi}{\pi}}[3(\Upsilon_1 - q_m \Upsilon_0) + 8\xi(\frac{\partial \Upsilon_1}{\partial \xi} - q_m \frac{\partial \Upsilon_0}{\partial \xi})] \tag{2.40}$$

$$Y_2 = -\frac{q_m}{2}\sqrt{\frac{j\xi}{\pi}}[3\Upsilon_0 + (\frac{j3}{2m_t^2} + 8\xi)\frac{\partial \Upsilon_0}{\partial \xi}]. \tag{2.41}$$

B. Electric Source Excitation

For the electric source excitation, using a formulation similar to the procedure presented in [14], the tangential surface field excited by a tangential electric source can be derived for the same geometry. Firstly, $\hat{z}$ components of electric and magnetic fields due to a tangential electric source

$$\vec{P}_e = P_e^z \hat{z} + P_e^\phi \hat{\phi} \tag{2.42}$$

located on the surface is derived in Appendix A as

$$\begin{aligned} E_z &= -\frac{Z_s}{4\pi^2 a}\int_{-\infty}^{\infty} dk_z e^{-jk_z z_d} \sum_{n=-\infty}^{\infty} \frac{e^{jn\phi_d}}{D_c}[(1+\frac{j\Lambda^{-1}k}{k_\rho}R_n)P_e^z + \frac{nk_z}{k_\rho^2 a}P_e^\phi] \\ &\quad \frac{H_n^{(2)}(k_\rho \rho)}{H_n^{(2)}(k_\rho a)} \qquad (2.43) \\ H_z &= \frac{1}{4\pi^2 a}\int_{-\infty}^{\infty} dk_z e^{-jk_z z_d} \sum_{n=-\infty}^{\infty} \frac{e^{jn\phi_d}}{D_c}[\frac{nk_z}{k_\rho^2 a}P_e^z + (1+\frac{j\Lambda k}{k_\rho}R_n)P_e^\phi] \\ &\quad \frac{H_n^{(2)}(k_\rho \rho)}{H_n^{(2)}(k_\rho a)}. \qquad (2.44) \end{aligned}$$

As expected, the $\hat{z}$ components of the fields (E_z, H_z) are the dual of the $\hat{z}$ components of the fields obtained for the magnetic source case in [14].

Once the $\hat{z}$ components of the fields (E_z, H_z) are obtained, the vector potentials (A_z, F_z) due to these components can easily be found using the methods described in [20]. Then, the procedure for the development of high frequency solutions, which is explained in [14], is followed. The details of the procedure are given in Appendix B.

As a result, the tangential surface field excited by a tangential electric source given by (2.42) is expressed as

$$\vec{H}_t = \vec{P}_e \cdot (\hat{z}'\hat{z}G_{zz}^e + \hat{\phi}'\hat{z}G_{z\phi}^e + \hat{z}'\hat{\phi}G_{\phi z}^e + \hat{\phi}'\hat{\phi}G_{\phi\phi}^e) \qquad (2.45)$$

where G_{pq}^e is a UTD based Green's function representation for a $\hat{p}$ ($\hat{p} = \hat{z}$ or $\hat{\phi}$) oriented surface magnetic field due to a $\hat{q}$ ($\hat{q} = \hat{z}$ or $\hat{\phi}$) directed electric current. Note that by relating the electric current to the magnetic field as in (2.45), the Green's function representation G_{pq}^e is defined to have a unit of $1/m^2$. Similar to the magnetic case in (2.45) G_{pq}^e contains the summation of all ray encirclements around the cylinder. However, only the leading term (i.e. $\ell = 0$) is retained. Finally, the explicit expressions for the UTD based asymptotic Green's function representations for various source and field orientations for the electric case are given by

$$G_{zz}^{e\pm} \sim \pm Z_s G_0\{\cos\alpha\sin\alpha[1-\frac{j3}{ks}(1-\frac{j}{ks})]Y_0 + [\frac{j}{3ks}(\tan^2\alpha+\frac{j}{ks})$$

$$
\begin{aligned}
& \cos\alpha\sin\alpha - \frac{\tan\alpha\cos 2\alpha}{6k^2s^2}]Y_1 + \frac{\tan\alpha\sin^2\alpha}{36k^2s^2}Y_2\} & (2.46) \\
G^{e\pm}_{z\phi} \sim\; & Z_sG_0\{\cos^2\alpha V_0 + \frac{j}{ks}(1-\frac{j}{ks})(2-3\cos^2\alpha)V_0 + [\frac{j}{3ks}(1-\frac{j}{ks}) \\
& \sin^2\alpha - \frac{\cos 2\alpha}{36k^2s^2}]V_1 + \frac{\sin^2\alpha}{36k^2s^2}V_2\} & (2.47) \\
G^{e\pm}_{\phi z} \sim\; & -Z_sG_0\{\sin^2\alpha Y_0 + \frac{j}{ks}(1-\frac{j}{ks})(2-3\sin^2\alpha)Y_0 + \frac{j}{ks}\frac{1}{\cos^2\alpha}(U_0 - Y_0) \\
& +[\frac{j}{ks}(1-\frac{j}{ks})(\frac{\cos^2\alpha - \sin^2\alpha - 4}{6s}) - \frac{j}{6s}(\cos\alpha - \frac{4}{\cos\alpha} \\
& -\frac{j}{ks}\tan\alpha\sin\alpha) - \frac{\tan\alpha\sin 2\alpha}{6k^2s^2}]Y_1 - (\frac{\sin^2\alpha + 4\tan^2\alpha}{36k^2s^2})Y_2\} & (2.48) \\
G^{e\pm}_{\phi\phi} \sim\; & \mp Z_sG_0\{\cos\alpha\sin\alpha[X_0 + V_0 - \frac{j3}{ks}(1-\frac{j}{ks})V_0] + [\frac{j}{k}(1-\frac{j}{ks})(\frac{2\tan\alpha}{3s} \\
& -\frac{\cos\alpha\sin\alpha}{3s}) - \frac{\sin 2\alpha}{6k^2s^2}]V_1 - \frac{\sin\alpha}{36s^2}(\cos\alpha - \frac{4}{\cos\alpha})V_2\} & (2.49)
\end{aligned}
$$

where U_0, X_0, V_0, Y_0, V_1, Y_1, V_2, Y_2 are the same functions given by (2.34)-(2.41). It should be mentioned that if G^e_{pq} was defined to relate the electric current density to the electric field (i.e. right hand side of (2.45) would be $\vec{E}_t$), then G^e_{pq} could also be determined via duality.

Similar to the magnetic source case, expressions given in (2.46)-(2.49) are valid in the non-paraxial region, and developed mainly for large separations between the source and field points. However, they may also remain accurate for relatively small separations due to the second order terms in s.

2.2.2 Solution to the Surface Fields in the Paraxial Region (Paraxial Solution)

The asymptotic solution given in the previous section cannot be used in the paraxial region of a circular cylinder because the Airy function approximation for Hankel function is not valid as $\alpha \to 90°$. For this reason, an alternative approximate closed-form solution is proposed in [14].

A. Magnetic Source Excitation

Green's function representations for various source and field orientations are given in [14] as

$$
\begin{aligned}
G^c_{zz} &\approx -\frac{1}{4\pi^2 Z_s a}\int_{-\infty}^{\infty} dk_z e^{-jk_z z_d}\int_{-\infty}^{\infty} d\nu e^{-j\nu\phi_d}\frac{N^c_{zz}}{D_c} && (2.50)\\
G^c_{z\phi} &= G^c_{\phi z}\\
&\approx \frac{1}{4\pi^2 Z_s a}\int_{-\infty}^{\infty} dk_z e^{-jk_z z_d}\int_{-\infty}^{\infty} d\nu e^{-j\nu\phi_d}\frac{N^c_{z\phi}}{D_c} && (2.51)\\
G^c_{\phi\phi} &\approx -\frac{1}{4\pi^2 Z_s a}\int_{-\infty}^{\infty} dk_z e^{-jk_z z_d}\int_{-\infty}^{\infty} d\nu e^{-j\nu\phi_d}(1-\frac{N^c_{\phi\phi}}{D_c}) && (2.52)
\end{aligned}
$$

where

$$
\begin{aligned}
N^c_{zz} &= 1+\frac{j\Lambda k}{k_\rho}R_\nu && (2.53)\\
N^c_{z\phi} &= \frac{\nu k_z}{k_\rho^2 a} && (2.54)\\
N^c_{\phi\phi} &= 1+\frac{j\Lambda^{-1}k}{k_\rho}R_\nu && (2.55)
\end{aligned}
$$

$$D_c = N^c_{zz}N^c_{\phi\phi} + (N^c_{z\phi})^2 \quad (2.56)$$

$$R_\nu = \frac{H^{(2)'}_\nu(k_\rho a)}{H^{(2)}_\nu(k_\rho a)}. \quad (2.57)$$

In this proposed solution, a two-term Debye expansion for R_ν, which is valid in the paraxial region,

$$R_\nu = -\frac{j\sqrt{k_\rho^2 a^2-\nu^2}}{k_\rho a} - \frac{k_\rho a}{2(k_\rho^2 a^2-\nu^2)} \quad (2.58)$$

is used instead of Airy function approximation. After employing the substitutions $\nu = k_y a$, and $y_d = a\phi_d$, and neglecting the higher powers of a^{-1} (since the radius of the cylinder is electrically large), Green's function representations are decomposed into two parts as

$$G^c_{pq} = G^f_{pq} + G^a_{pq}. \quad (2.59)$$

Using the definition $k_x = -j\sqrt{k_y^2+k_z^2-k^2}$ and introducing a standard polar transformation of the form

$$k_y = k_s\cos\psi, \qquad k_z = k_s\sin\psi \quad (2.60)$$

along with the geometrical properties $y_d = s\cos\alpha$ and $z_d = s\sin\alpha$, one of the integrals within the spectral double integrals involved in the Green's function representations is evaluated in exact fashion using the integral identity

$$\int_0^{2\pi} d\psi e^{-jk_s s\cos(\psi-\alpha)} = 2\pi J_0(k_s s). \tag{2.61}$$

Moreover, the range of the other integral is changed from $(0,\infty)$ to $(-\infty,\infty)$ by expressing the Bessel function in (2.61) as a combination of Hankel functions of the first and second kinds. Since, there is no α variation in the resulting integral, the derivatives with respect to the azimuthal separation, y_d, and the axial separation, z_d can be interchanged by those with the path length, s, using the relationship $s = \sqrt{y_d^2 + z_d^2}$. Then, the Green's function representations are put into their final form in [14] as

$$G^f_{zz} \approx -\frac{1}{4\pi^2 Z_0 k}[k^2 P(\Lambda) + (\frac{\cos^2\alpha}{s}\frac{\partial}{\partial s} + \sin^2\alpha\frac{\partial^2}{\partial s^2})Q] \tag{2.62}$$

$$G^f_{z\phi} \approx \frac{1}{4\pi^2 Z_0 k}\cos\alpha\sin\alpha(\frac{1}{s}\frac{\partial}{\partial s} - \frac{\partial^2}{\partial s^2})Q \tag{2.63}$$

$$G^f_{\phi\phi} \approx -\frac{1}{4\pi^2 Z_0 k}[k^2 P(\Lambda) + (\frac{\sin^2\alpha}{s}\frac{\partial}{\partial s} + \cos^2\alpha\frac{\partial^2}{\partial s^2})Q] \tag{2.64}$$

and

$$\begin{aligned} G^a_{zz} \approx\ & \frac{j}{8\pi^2 Z_0 ka}\{(\frac{\cos^2\alpha}{s}\frac{\partial}{\partial s} + \sin^2\alpha\frac{\partial^2}{\partial s^2})R(\Lambda^{-1}) - \cos 4\alpha[\frac{1}{s}\frac{\partial T}{\partial s} \\ & -\frac{3}{k^2 s^2}(\frac{1}{s}\frac{\partial}{\partial s} - \frac{\partial^2}{\partial s^2})S] - \frac{\sin^2 2\alpha}{4}(\frac{1}{s}\frac{\partial}{\partial s} + \frac{\partial^2}{\partial s^2})T\} \end{aligned} \tag{2.65}$$

$$\begin{aligned} G^a_{z\phi} \approx\ & \frac{j}{8\pi^2 Z_0 ka}\{\sin 4\alpha[\frac{1}{s}\frac{\partial T}{\partial s} - \frac{3}{k^2 s^2}(\frac{1}{s}\frac{\partial}{\partial s} - \frac{\partial^2}{\partial s^2})S] \\ & \frac{\sin 2\alpha}{2}(\frac{\cos^2\alpha}{s}\frac{\partial}{\partial s} + \sin^2\alpha\frac{\partial^2}{\partial s^2})T\} \end{aligned} \tag{2.66}$$

$$\begin{aligned} G^a_{\phi\phi} \approx\ & \frac{j}{8\pi^2 Z_0 ka}\{k^2 L - (\frac{\cos^2\alpha}{s}\frac{\partial}{\partial s} + \sin^2\alpha\frac{\partial^2}{\partial s^2})R(\Lambda) + \cos 4\alpha[\frac{1}{s}\frac{\partial T}{\partial s} \\ & -\frac{3}{k^2 s^2}(\frac{1}{s}\frac{\partial}{\partial s} - \frac{\partial^2}{\partial s^2})S] + \frac{\sin^2 2\alpha}{4}(\frac{1}{s}\frac{\partial}{\partial s} + \frac{\partial^2}{\partial s^2})T\} \end{aligned} \tag{2.67}$$

where

$$P(\Omega) = I_1(\Omega) + \frac{j}{2a}I_3(\Omega) \tag{2.68}$$

$$
\begin{aligned}
Q &= \frac{1}{1-\Lambda^2}[P(\Lambda) - P(\Lambda^{-1})] && (2.69)\\
R(\Omega) &= -\frac{\Omega}{\Lambda(1-\Omega^2)}[I_2(0) - \frac{1}{1-\Omega^2}I_2(\Omega) + \frac{\Omega^2}{1-\Omega^2}I_2(\Omega^{-1}) \\
&\quad -(1+\Omega^2)I_3(\Omega)] && (2.70)\\
L &= \frac{1}{1-\Lambda^2}[I_2(\Lambda) - I_2(\Lambda^{-1})] && (2.71)\\
T &= \frac{1+\Lambda^2}{1-\Lambda^2}[I_3(\Lambda) - \Lambda^{-2}I_3(\Lambda^{-1})] && (2.72)\\
S &= -\frac{1+\Lambda^2}{(1-\Lambda^2)^2}[I_2(0) - \frac{1}{1-\Lambda^2}I_2(\Lambda) + \frac{\Lambda^2}{1-\Lambda^2}I_2(\Lambda^{-1}) \\
&\quad -I_3(\Lambda) - I_3(\Lambda^{-1})] && (2.73)
\end{aligned}
$$

in which Ω is either Λ or Λ^{-1}, I_1, I_2, andI_3 are the spectral integrals defined as

$$
\begin{aligned}
I_1(\Omega) &= \pi\int_{-\infty}^{\infty} dk_s H_0^{(2)}(k_s s)\frac{k_s}{k_x+\Omega k} && (2.74)\\
I_2(\Omega) &= \pi\int_{-\infty}^{\infty} dk_s H_0^{(2)}(k_s s)\frac{2k_s}{k_x(k_x+\Omega k)} && (2.75)\\
I_3(\Omega) &= \pi\int_{-\infty}^{\infty} dk_s H_0^{(2)}(k_s s)\frac{k^2 k_s}{k_x^2(k_x+\Omega k)^2}. && (2.76)
\end{aligned}
$$

Chapter 3

Numerical Evaluation of Surface Fields

3.1 Two-Dimensional Case/Three-Dimensional Case (Non-paraxial Region)

The major difficulty in the evaluation of (2.4), (2.12), (2.21)-(2.24), and (2.46)-(2.49) is the numerical evaluation of the Fock type integrals given in (2.8) and (2.25). Since the accuracy and efficiency of the surface fields strongly depend on these integrals, special care is required for their numerical evaluation. Therefore, in this section, the approach presented in [11] and [14] is briefly reviewed (as Residue Series Approach), and then the alternative approach named as the Numerical Integration Approach is presented.

A. Residue Series Approach

This approach is based on invoking the Cauchy's residue theorem for the evaluation of the Fock type integrals. The values of integrals are obtained by summing the residues at the pole singularities of the integrands.

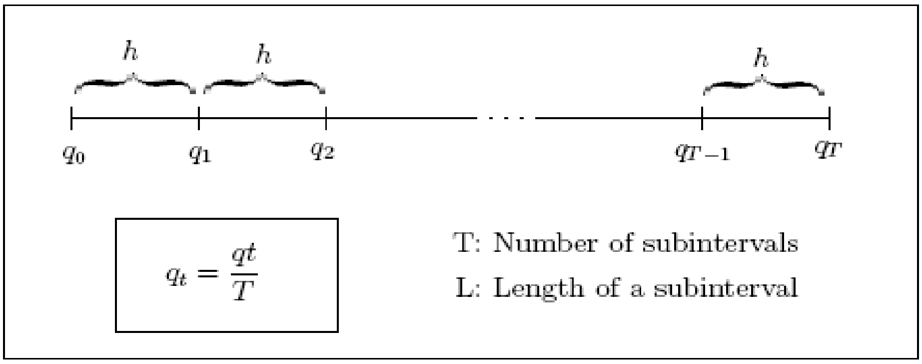

Figure 3.1: Definition of uniformly spaced points, q_t.

To apply the Cauchy's residue theorem, the root locations of the denominator should be determined. For the line source excitation (TE_z, and TM_z case), the roots satisfy

$$R_w - q\Big|_{\tau=\tau_i} = 0. \tag{3.1}$$

The numerical procedure for finding the roots of (3.1) is presented in [14]. Briefly, using the Airy Differential equation

$$W_2''(\tau) - \tau W_2(\tau) = 0 \tag{3.2}$$

and the derivative of (3.1), we have the following equations

$$\frac{\partial \tau_i}{\partial q} = \frac{1}{\tau_i - q^2}, \quad \tau_i\Big|_{q=0} = -\alpha_i' e^{-j\pi/3}, \quad for\ |q| \leq 1 \tag{3.3}$$

$$\frac{\partial \tau_i}{\partial \hat{q}} = \frac{1}{1 - \hat{q}^2 \tau_i}, \quad \tau_i\Big|_{\hat{q}=0} = -\alpha_i e^{-j\pi/3}, \quad for\ |q| > 1 \tag{3.4}$$

with $\hat{q} = 1/q$, α_i and α_i' are one of the infinitely many zeros of Airy function and its derivative with respect to its argument, respectively. The first twenty roots of the Airy function and its derivative with respect to its argument are given in Table 3.1.

For $|q| \leq 1$ case, the interval $[0, q]$ is divided into T equally spaced subintervals having a length of h as shown in Fig. 3.1. T is chosen as the largest integer, which does not exceed $1 + 100|q|$, so that $|h| < 0.01$. Then, (3.3) is integrated from q_0

i	α_i	α'_i		i	α_i	α'_i
1	-2.33810741	-1.01879297		11	-13.69148904	-13.26221896
2	-4.08794944	-3.24819758		12	-14.52782995	-14.11150197
3	-5.52055983	-4.82009921		13	-15.34075514	-14.9359372
4	-6.78670809	-6.16330736		14	-16.13268516	-15.73820137
5	-7.94413359	-7.37217726		15	-16.905634	-16.52050383
6	-9.02265085	-8.48848673		16	-17.66130011	-17.28469505
7	-10.04017434	-9.53544905		17	-18.4011326	-18.03234462
8	-11.0085243	-10.5276604		18	-19.12638047	-18.76479844
9	-11.93601556	-11.47505663		19	-19.83812989	-19.48322166
10	-12.82877675	-12.38478837		20	-20.53733291	-20.18863151

Table 3.1: The first twenty roots of Airy function and its derivative with respect to its argument

to q_T using the fourth order Runge Kutta method as [21]

$$\tau_i(q_{t+1}) = \tau_i(q_t) + \frac{h}{6}[y_1 + 2(y_2 + y_3) + y_4] \tag{3.5}$$

which is computed recursively from $t = 0$ to $t = T - 1$

$$y_1 = \Phi[q_t, \tau_i(q_t)] \tag{3.6}$$

$$y_2 = \Phi[q_t + \frac{h}{2}, \tau_i(q_t) + \frac{y_1}{2}] \tag{3.7}$$

$$y_3 = \Phi[q_t + \frac{h}{2}, \tau_i(q_t) + \frac{y_2}{2}] \tag{3.8}$$

$$y_4 = \Phi[q_t + h, \tau_i(q_t) + y_3] \tag{3.9}$$

where

$$\Phi(q, \tau) = \frac{1}{\tau - q^2}. \tag{3.10}$$

For $|q| > 1$ case, (3.4) is integrated using the same procedure above except q, and Φ are replaced with $\hat{q}$, and $\hat{\Phi}$ such that

$$\hat{\Phi}(\hat{q}, \tau) = \frac{1}{1 - \hat{q}^2\tau}. \tag{3.11}$$

Using the Cauchy's residue theorem, the Fock type integral for 2-D case, (2.8), can be represented as follows:

$$\nu(\xi,q)=\begin{cases} -j2\pi\sum_{i=1}^{\infty}\frac{e^{-j\xi\tau}}{\tau-q^2}\Big|_{\tau=\tau_i} & \text{if } |q|\le 1\\ -j2\pi\sum_{i=1}^{\infty}\frac{e^{-j\xi\tau}}{1-\hat{q}^2\tau}\Big|_{\tau=\tau_i} & \text{if } |q|>1.\end{cases} \tag{3.12}$$

The first two roots are included to obtain accurate results.

For the 3-D case, the root locations of the denominator D_w cannot be determined easily because of the coupling term, which varies with τ. To determine these roots, D_w is written in [14] in the following form:

$$D_w = Q_e(\tau)Q_m(\tau) \tag{3.13}$$

where

$$Q_e(\tau) = R_w - q_e + \sigma \tag{3.14}$$

$$Q_m(\tau) = R_w - q_m - \sigma \tag{3.15}$$

$$\sigma = \frac{q_e - q_m - \sqrt{(q_e-q_m)^2 - 4q_c^2}}{2}, \tag{3.16}$$

with the root having the positive real part is chosen. The roots of Q_e, namely $\tau_{p\,i_1}$, are determined by applying Newton-Raphson method. In this method, an initial estimate for the locations of the roots is required, and this estimate must be close to the original location of the roots. For this reason, as an initial estimate, the roots of $(R_w - q_e)$ are obtained using the root finding procedure for the 2-D case, which is explained above. Then, the roots are tracked from $(R_w - q_e)$ to Q_e using a step by step procedure as described in [14]. The roots of Q_m, namely $\tau_{p\,i_2}$, are determined in a similar manner. Finally, using the Cauchy's residue theorem, the Fock type integral in (2.25) is represented as follows

$$\begin{aligned}\Upsilon_r &= -j2\pi\sum_{i=1}^{\infty}[e^{-j\xi\tau}\frac{(R_w)^r}{Q_e'(\tau)Q_m(\tau)}\Big|_{\tau=\tau_{p\,i_1}} + e^{-j\xi\tau}\frac{(R_w)^r}{Q_e(\tau)Q_m'(\tau)}\Big|_{\tau=\tau_{p\,i_2}}]\\ &= -j2\pi\sum_{i=1}^{\infty}\{e^{-j\xi\tau}\frac{(q_e-\sigma)^r}{[\tau-(q_e-\sigma)^2+\sigma'](q_e-q_m-2\sigma)}\Big|_{\tau=\tau_{p\,i_1}}\\ &\quad +e^{-j\xi\tau}\frac{(q_m+\sigma)^r}{(q_m-q_e+2\sigma)[\tau-(q_m+\sigma)^2-\sigma']}\Big|_{\tau=\tau_{p\,i_2}}\}\end{aligned} \tag{3.17}$$

where Q'_e, Q'_m and σ' are the derivatives of Q_e, Q_m and σ with respect to τ, respectively. The first 20 roots (20 for Q_e and 20 for Q_m) are included to obtain accurate results as suggested in [14].

B. Numerical Integration Approach

This approach is based on performing a numerical integration for the evaluation of the Fock type integrals. The original integration path for the Fock type integrals given by (2.8) and (2.25) ranges from $-\infty$ to ∞ on the complex τ-plane, as shown in Fig. 3.2(a), where τ is the integration variable. Unfortunately, the integrals may not converge rapidly when this path is used since the integrands have a highly oscillatory and slowly convergent behavior. This is illustrated in Fig. 3.3, where the variation of the real and imaginary parts of the integrand of a typical Fock type integral (Υ_1) versus τ is depicted. Therefore, these integrals are evaluated on a deformed path similar to the one in [18]-[19]. Note that, various types of deformed paths have been previously used for the coated cylinder case in [16]-[19], [22]. However, the path suggested in [18]-[19] seems to yield the best result for the evaluation of the Fock type integrals pertaining to a circular cylinder with an IBC. To obtain accurate results, the path deformation should be done carefully so that all pole singularities are captured. The poles are known to be in the second and fourth quadrants. The second quadrant poles are the negative of the fourth quadrant poles; only the fourth quadrant poles are shown in Fig. 3.2, where the poles of Υ_1 pertaining to an electrically large cylinder with $a = 5\lambda$, $\Lambda = 0.1$ at 7 GHz are determined for $s = 1\lambda$, $\alpha = \pi/4$. Since there is no pole in the third quadrant, part of the integration path ranging from $-\infty$ to 0 can be safely deformed to the third quadrant. However, special attention is required in deforming the part of the integration path ranging from 0 to ∞ into the fourth quadrant because of the existence of the pole singularities. As the pole locations in this quadrant are similar to [18]-[19], the critical issues manifest themselves in the location of the first (dominant) pole and in the slope of the pole location trajectories. It is seen that the dominant pole has the closest location to the integration path and may come very close to the real τ-axis thereby giving rise to a low-attenuation Elliott mode for some surface impedance values

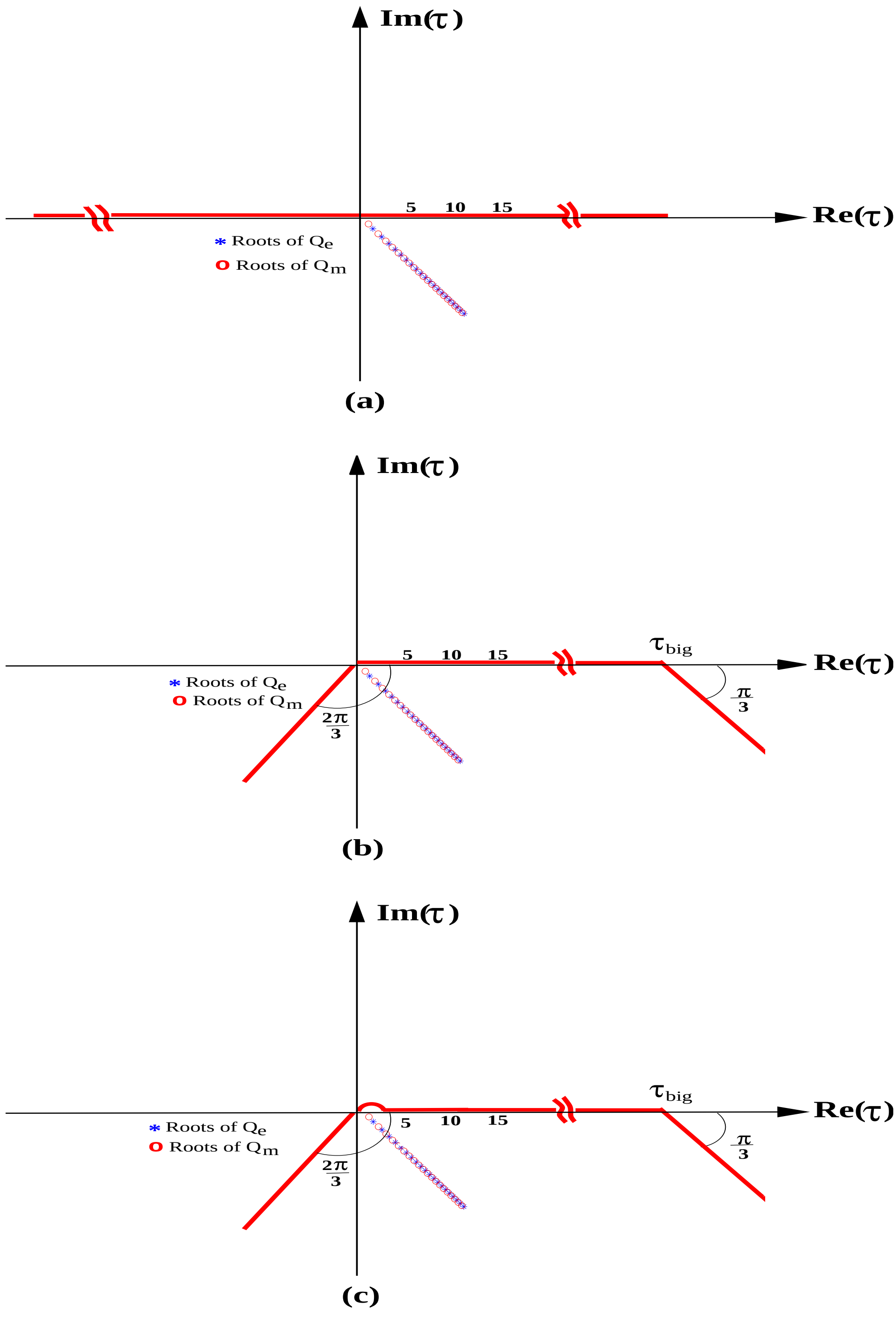

Figure 3.2: Paths of integration (a) Original path. (b) Deformed path 1. (c) Deformed path 2, used when the dominant pole is very close to the integration path (like an Elliott mode).

Z_s [23]-[25]. Moreover, it has a real part significantly smaller than τ_{big} (defined on Fig. 3.2(b)). On the other hand, all remaining poles, which can be defined as $\tau_{p_i} = Re(\tau_{p_i}) - j\, Im(\tau_{p_i})$, $(i = 2, 3, 4, ...)$ are lined up on the 4th quadrant satisfying the following condition: $Re(\tau_{p_i}) < Re(\tau_{p_i+1})$ and $Im(\tau_{p_i}) < Im(\tau_{p_i+1})$, as shown in Fig. 3.2, and the slope of the pole location trajectory is approximately $\pi/3$ (defined from the positive real τ axis). Note that when $|\tau|$ is very large the trajectory approaches to $\pi/2$ (similar to PEC cylinders) [26].

In the light of above considerations, the Fock type integrals, whose generic form is given in (2.25), are split into three integrals ranging from $(-\infty, 0)$, $(0, \tau_{big})$, and (τ_{big}, ∞), where τ_{big} is chosen approximately $1.5k\,a$. Such a choice guarantees that all pole singularities corresponding to different cylinder size (varying between 3λ and 6λ) and different cylinder surface impedance values (varying between $|\Lambda| = 0.1$ and $|\Lambda| = 5$) studied in this thesis and in [14] are captured. Furthermore, as the frequency is increased, there will be relatively little change in the position of the poles that reside near the $e^{-j\pi/3}$ axis in the τ-plane. However, based on the location of the dominant pole, small adjustments can be done about the value of τ_{big} (even setting $\tau_{big} = k\,a$ captures all the poles for all cases studied in [14]). As the next step, the integration path for the first and third integrals are deformed to $(\infty e^{-j2\pi/3}, 0)$, and $(\tau_{big}, \infty e^{-j\pi/3})$, respectively. Then, the integration variable τ is changed to $\tau e^{j2\pi/3}$ for the first integral, and to $(\tau - \tau_{big})e^{j\pi/3}$ for the third integral resulting the Airy function and its derivative to be non oscillatory and decay most rapidly (an exponential decay is achieved) as $|\tau| \to \infty$ along the path where $arg(\tau) = 0$ [22]. Consequently, the first and the third integrals now range from 0 to ∞, they are fast decaying, non oscillatory. This is shown in Fig. 3.3, where the variation of the real and imaginary parts of the integrand of the Fock type integral Υ_1 versus $Re(\tau)$ (mentioned above) is plotted along the original and deformed paths for the aforementioned impedance cylinder (i.e. $a = 5\lambda$, $\Lambda = 0.1$, $f = 7\,GHz$, $s = 1\lambda$ and $\alpha = \pi/4$). The value of the integrand (both real and imaginary parts) for the first and the third integrals exponentially decay and go to zero. Although the integrand of the second integral is oscillatory, the integration interval is quite short and hence, its evaluation does not create a severe problem. Still, most of the CPU time is consumed during the computation

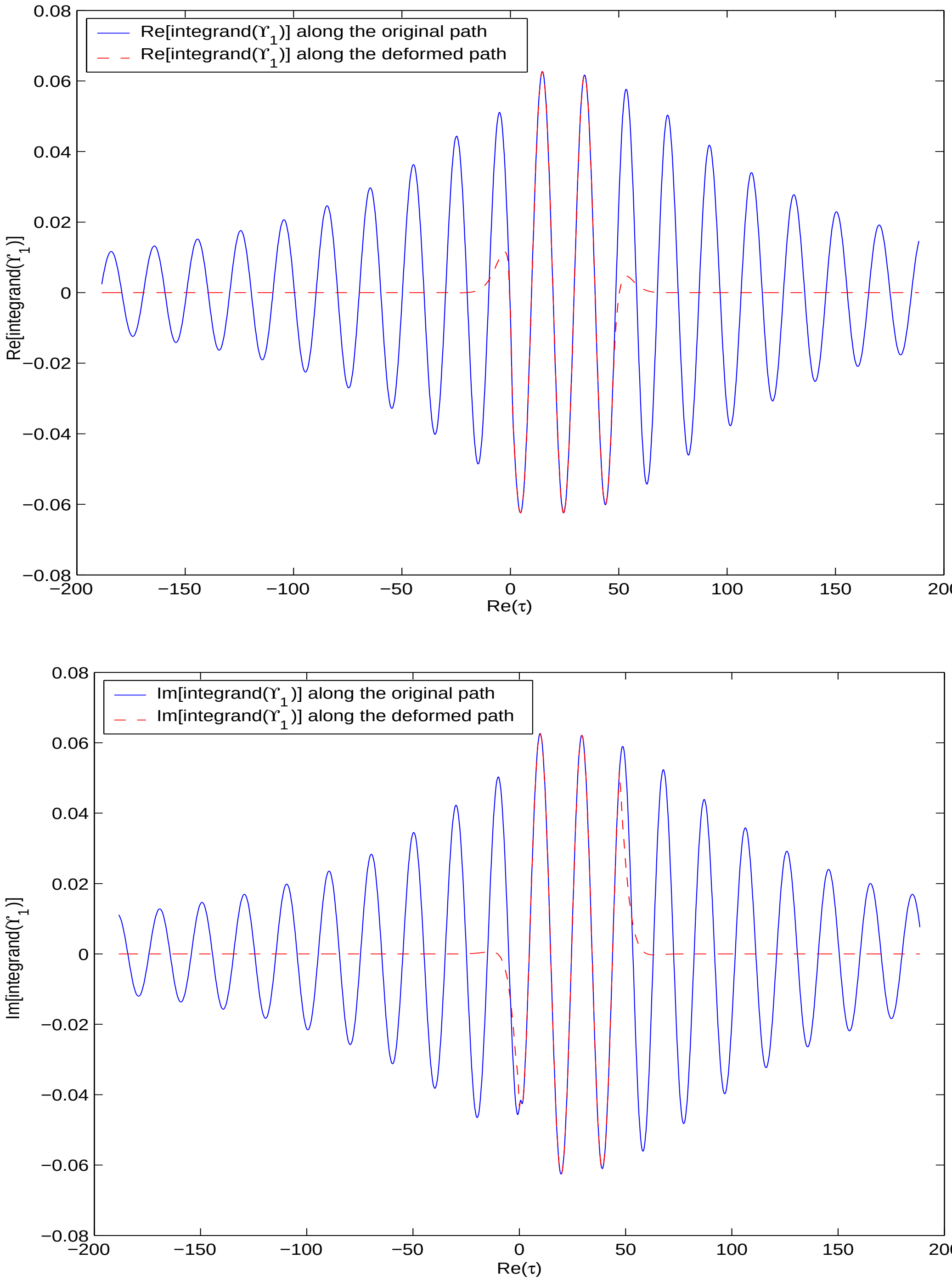

Figure 3.3: (a) Real and (b) Imaginary parts of integrand of a typical Fock type integral (in this case integrand of Υ_1) along the original and deformed paths.

of this second integral. Finally, all integrals can be integrated efficiently using a simple Gaussian quadrature algorithm. It should be noted that, in the case of a pole very close to the integration path, a small semicircle as shown in Fig. 3.2(c) is introduced.

As a final note, further improvement can be made for the computational time. Using the pole search algorithm explained in the previous section, the dominant pole is found. Based on the location of the dominant pole, τ_{big} can be adjusted to have a smaller value than $1.5k\,a$. Although finding the dominant pole brings extra burden in the computation, time consumption is considerably reduced in the computation of the second integral.

3.2 Three-Dimensional Case (Paraxial Region)

In this section, the evaluation of the paraxial solution for the magnetic field excited by a magnetic point source, which is discussed in the previous chapter, is briefly reviewed.

The spectral integrals, (2.74)-(2.76), do not seem to be integrable in closed-form. Since the parameter, $k_s s$, is large, using the large argument representation of the zeroth order Hankel function

$$\lim_{k_s s \to \infty} H_0^{(2)}(k_s s) \sim \sqrt{\frac{j2}{\pi k_s s}} e^{-jk_s s} \tag{3.18}$$

the spectral integrals can be evaluated approximately.

Employing the variable transformations

$$k_s = k - \frac{j\gamma^2}{s}, \quad \sqrt{k_s} \sim \sqrt{k}, \quad k_x \sim -j\sqrt{\frac{j2k}{s}}\gamma \tag{3.19}$$

to (2.74)-(2.76), following equations are obtained in [14]

$$\begin{aligned} I_i(\Omega) &\sim \pi e^{-jks}\varphi_{i1} & (3.20)\\ \frac{\partial}{\partial s} I_i(\Omega) &\sim -j\pi k e^{-jks}[(1-\frac{j}{2ks})\varphi_{i1} + \frac{j\varphi_{i2}}{2ks}] & (3.21) \end{aligned}$$

$$
\begin{aligned}
\frac{\partial^2}{\partial s^2} I_i(\Omega) \sim & -\pi k^2 e^{-jks}[(1-\frac{j}{ks}-\frac{3}{4k^2s^2})\varphi_{i1}+(1-\frac{j}{2ks})\frac{j\varphi_{i2}}{ks} \\
& +\frac{j\varphi_{i3}}{4k^2s^2}]
\end{aligned} \tag{3.22}
$$

for $i = 1, 2, 3$ such that

$$\varphi_{11} = \frac{j2}{s}F(p) \tag{3.23}$$

$$\varphi_{21} = \frac{2}{\sqrt{p}}\sqrt{\frac{j2}{ks}}[1-F(p)] \tag{3.24}$$

$$\varphi_{31} = \frac{j}{p\sqrt{p}}\sqrt{\frac{jks}{2}}[1-j\sqrt{\pi p}-(1+2p)F(p)] \tag{3.25}$$

$$\varphi_{12} = -\frac{j2}{s}[1+2pF(p)] \tag{3.26}$$

$$\varphi_{22} = 4\sqrt{p}\sqrt{\frac{j2}{ks}}F(p) \tag{3.27}$$

$$\varphi_{32} = \frac{j2}{\sqrt{p}}\sqrt{\frac{jks}{2}}[1-(1-2p)F(p)] \tag{3.28}$$

$$\varphi_{13} = -\frac{j2}{s}[3+2p+4p^2F(p)] \tag{3.29}$$

$$\varphi_{23} = 4\sqrt{p}\sqrt{\frac{j2}{ks}}[1+2pF(p)] \tag{3.30}$$

$$\varphi_{33} = j4\sqrt{p}\sqrt{\frac{jks}{2}}[1-(3-2p)F(p)] \tag{3.31}$$

where $F(p)$, and $\frac{\partial F(p)}{\partial s}$ are transition function and its derivative respectively such that

$$F(p) = 1 - j\sqrt{\pi p}e^{-p}erfc(j\sqrt{p}) \tag{3.32}$$

$$\frac{\partial F(p)}{\partial s} = \frac{1}{2s}[(1-2p)F(p)-1] \tag{3.33}$$

in which $erfc$ is the complementary error function and $p = -\frac{j\Omega^2 ks}{2}$.

Transition function is evaluated in [14] as

$$
F(p) = \begin{cases}
\sqrt{p}\sum_{m=0}^{\infty}\frac{(-j\sqrt{p})^m}{\Gamma[\frac{(m+1)}{2}]} & \text{if } |p| \le 10 \\
-\sum_{m=0}^{\infty}\frac{1\cdot 3\cdots(2m-1)}{(2p)^m} & \text{if } |p| > 10,\ -3\pi/2 \le \angle p \le 0 \\
-j2\sqrt{\pi p}e^{-p}-\sum_{m=0}^{\infty}\frac{1\cdot 3\cdots(2m-1)}{(2p)^m} & \text{if } |p| > 10,\ 0 \le \angle p \le \pi/2
\end{cases} \tag{3.34}
$$

where $\Gamma(z+1) = z\Gamma(z)$ with $\Gamma(1/2) = \sqrt{\pi}$, and $\Gamma(1) = 1$.

It should be noted that the proper branch for $\sqrt{p}$ ($Im(\sqrt{p}) < 0$) has to be chosen so that radiation condition is satisfied.

Chapter 4

Numerical Results

In this section, several numerical results for the surface fields for both 2-D and 3-D cases are given to illustrate the accuracy and efficiency of the asymptotic solutions.

Firstly, Green's function for the 2-D case (TE/TM) is calculated using the residue series approach and the numerical integration approach for the cylinder given in Fig. 2.1 having a radius $a = 5\lambda/2$ ($ka = 5$). The magnitude of the Green's function are plotted in Fig. 4.1. It is seen from the figure that both approaches yield a very good agreement with each other.

Surface fields in the non-paraxial region due to both magnetic and electric sources are obtained using the aforementioned numerical approaches and compared with the eigenfunction solution. The eigenfunction solution for the surface fields due to the magnetic source is given in [14], and the solution due to the electric source is the dual of the magnetic source case.

Various components of Green's function representations are computed for the geodesic path length varying from 0.1λ to 5λ at $f = 7\,GHz$ on the aforementioned cylinder (with a radius 5λ, and a normalized surface impedance $\Lambda = 0.1$) for a fixed azimuthal angle ($\alpha = 45°$). The Fock type integrals in the Green's function representations are evaluated by (i) Cauchy's residue theorem (Residue Series

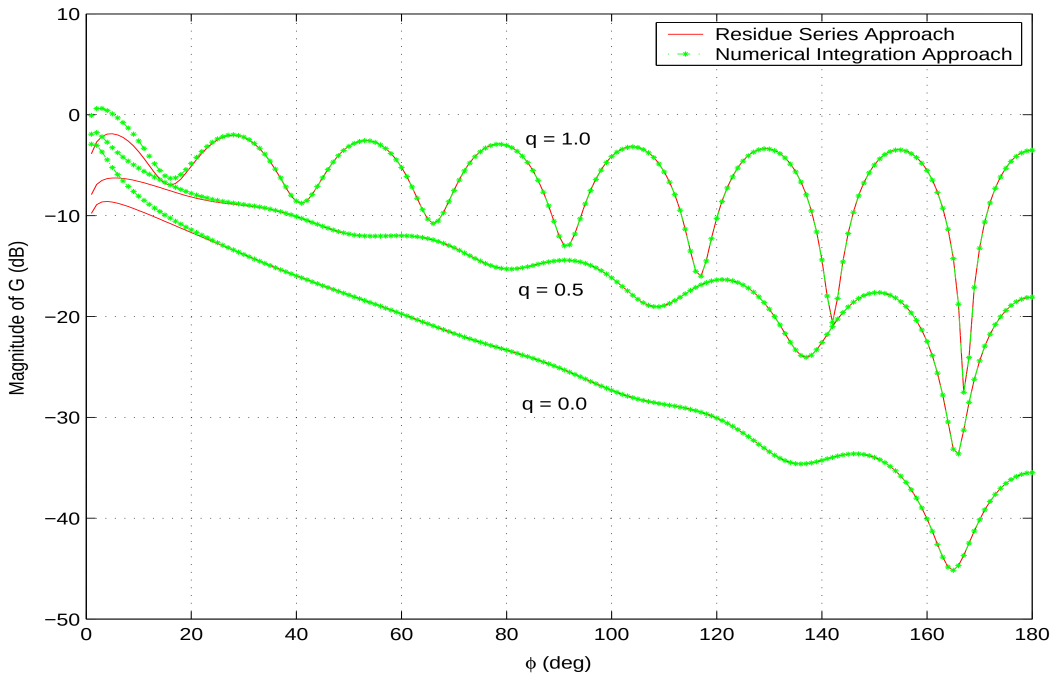

Figure 4.1: Comparison of the magnitude (in dB) of the Green's function (2-D case) versus azimuthal angle, ϕ, obtained by the the numerical approaches for $ka = 5$.

approach) and (ii) Numerical Integration Approach by setting τ_{big} to $1.5\,k\,a$. Note that because the cylinder is electrically large ($a > 1\lambda$), it is enough to retain the $\ell = 0$ term ([14]), which corresponds to the primary ray propagating around the cylinder. Therefore, in all numerical examples presented, only the leading term is retained.

Components of the Green's function representation due to a magnetic source (i.e. G^m_{pq}) obtained by these approaches are plotted in Fig. 4.2-4.4. Both approaches yield a very good agreement when compared with the eigenfunction solution given in [14] as illustrated in Fig. 4.2-4.4. It should be noted, however, that the numerical integration has several advantages over the Residue Series approach. Firstly, it is more efficient in terms of computational time as shown in Table 4.1. Secondly, locating the poles requires a difficult and a complex procedure. One can easily miss a pole, and/or pole search algorithms may need to be modified for some geometries and physical parameters. Finally, a finite number of poles are taken into consideration in Residue Series approach whereas all poles

	Residue Series Approach		Numerical Integration Approach	
	Mag. source	Elec. source	Mag. source	Elec. source
G_{zz}	92.2 sec.	89.5 sec.	19.8 sec.	19.7 sec.
$G_{z\phi}$	89.1 sec.	92.6 sec.	19.7 sec.	19.8 sec.
$G_{\phi\phi}$	89.7 sec.	89.6 sec.	29.6 sec.	19.7 sec.

Table 4.1: Computational Time

are included during the numerical integration.

Also, for the same geometry considered above, various components of Green's function representations due to an electric source (i.e. G^e_{pq}) are computed using both approaches and compared with the eigenfunction solution in Fig. 4.5-4.7. Both approaches are in very good agreement with the eigenfunction solution. However, similar to the magnetic source case, computation of surface fields using the Numerical Integration approach requires less CPU time as shown in Table 4.1.

It should be noted that although the developed UTD-based asymptotic Green's function representations (i.e. the surface fields) are derived for large separations between the source and field points, results are accurate even for relatively small separations. Small disagreements between the eigenfunction solution and the two approaches are due to the convergence problem of the eigenfunction solution, which is expected especially for large separations and clearly seen in all numerical results. On the other hand, the eigenfunction solution for the $G^m_{\phi\phi}$ component is the most slowly convergent component and such a slow convergence affects its agreement with the asymptotic solutions starting from approximately 0.5λ.

As it is explained before, the UTD based solution becomes less accurate in the paraxial region of the cylinder. This is illustrated in Fig. 4.8, which plots the UTD based Green's function representation for a $\hat{z}$ oriented surface magnetic field due to a $\hat{z}$ directed point magnetic current (G_{zz}) for the aforementioned geometry except for a different azimuthal angle ($\alpha = 80°$). However, the paraxial region solution is in good agreement with the eigenfunction solution. Small

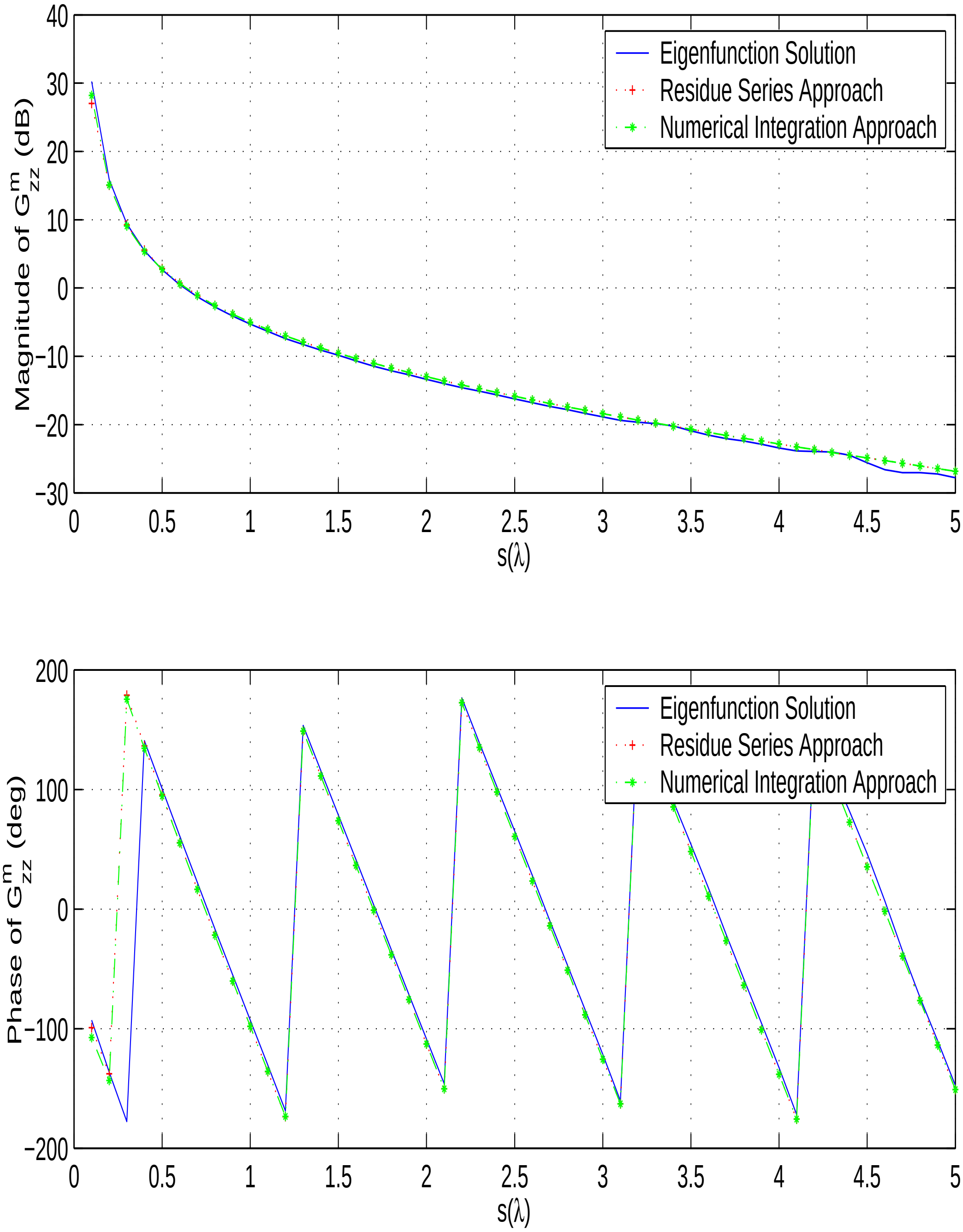

Figure 4.2: Comparison of the magnitude (in dB) and phase of the G_{zz}^m versus separation, s, obtained by the eigenfunction solution and the numerical approaches for $f = 7GHz$, $a = 5\lambda$, $\alpha = 45°$ and $\Lambda = 0.1$.

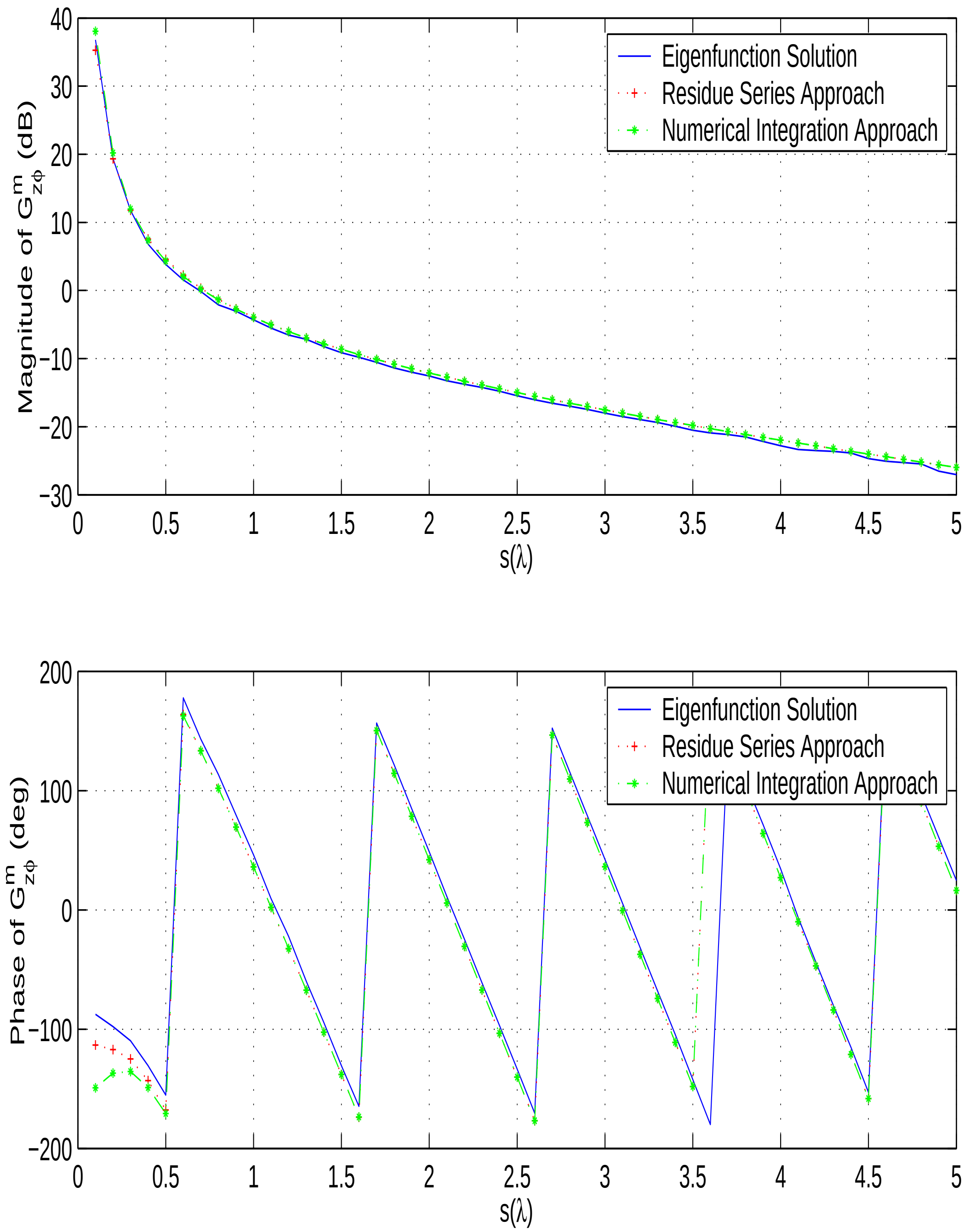

Figure 4.3: Comparison of the magnitude (in dB) and phase of the $G^m_{z\phi}$ versus separation, s, obtained by the eigenfunction solution and the numerical approaches for $f = 7GHz$, $a = 5\lambda$, $\alpha = 45°$ and $\Lambda = 0.1$.

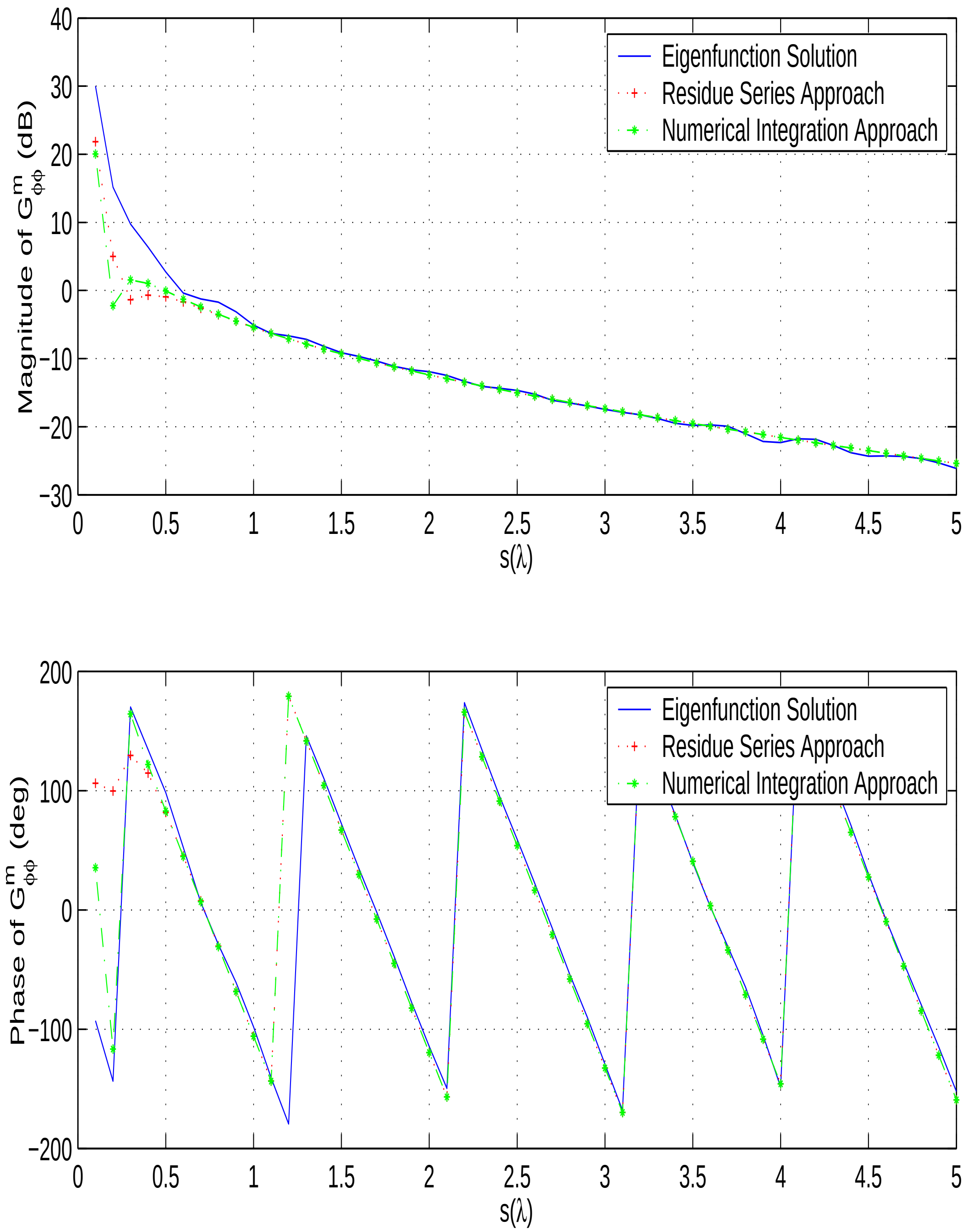

Figure 4.4: Comparison of the magnitude (in dB) and phase of the $G^m_{\phi\phi}$ versus separation, s, obtained by the eigenfunction solution and the numerical approaches for $f = 7GHz$, $a = 5\lambda$, $\alpha = 45°$ and $\Lambda = 0.1$.

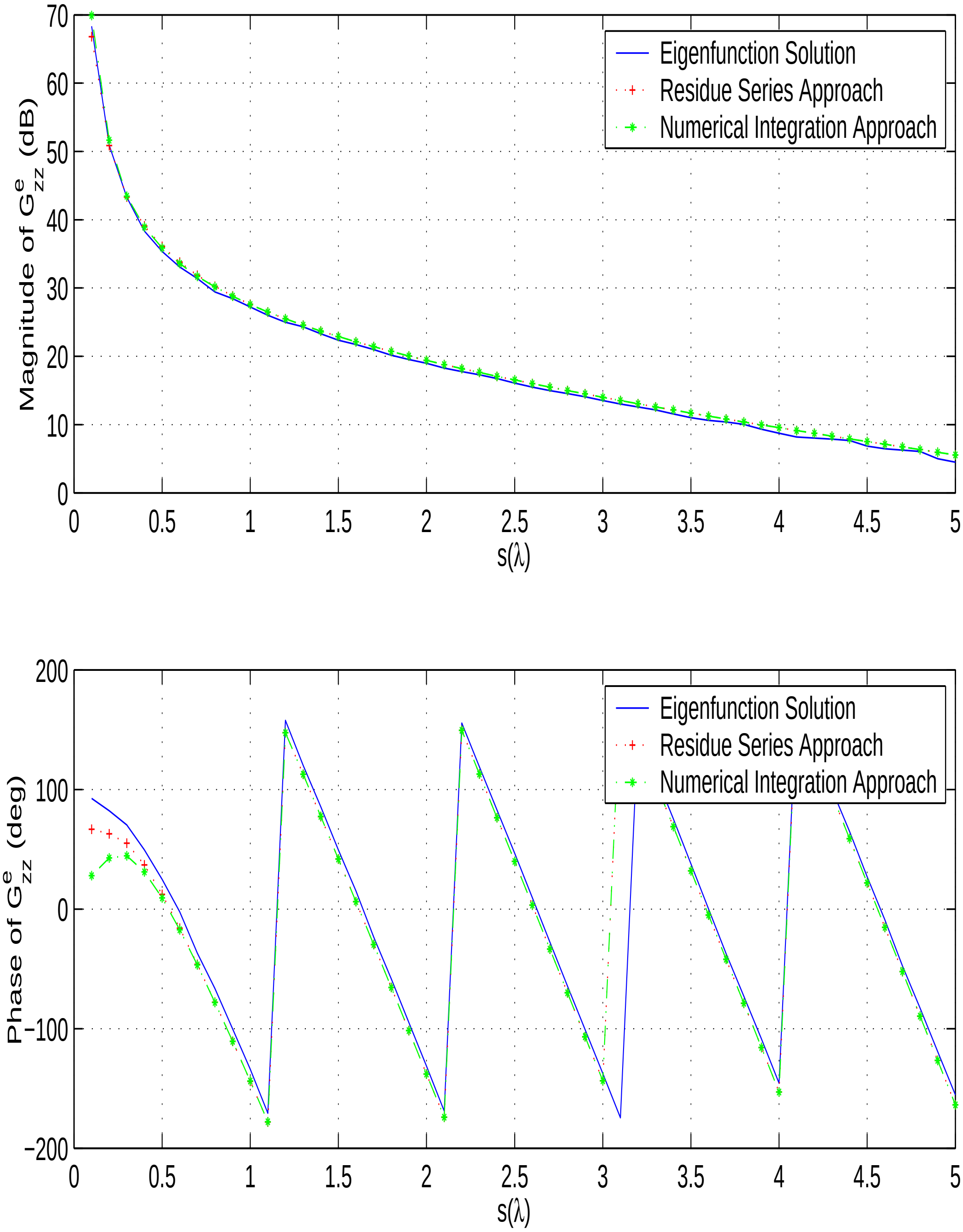

Figure 4.5: Comparison of the magnitude (in dB) and phase of the G^e_{zz} versus separation, s, obtained by the eigenfunction solution and the numerical approaches for $f = 7GHz$, $a = 5\lambda$, $\alpha = 45°$ and $\Lambda = 0.1$.

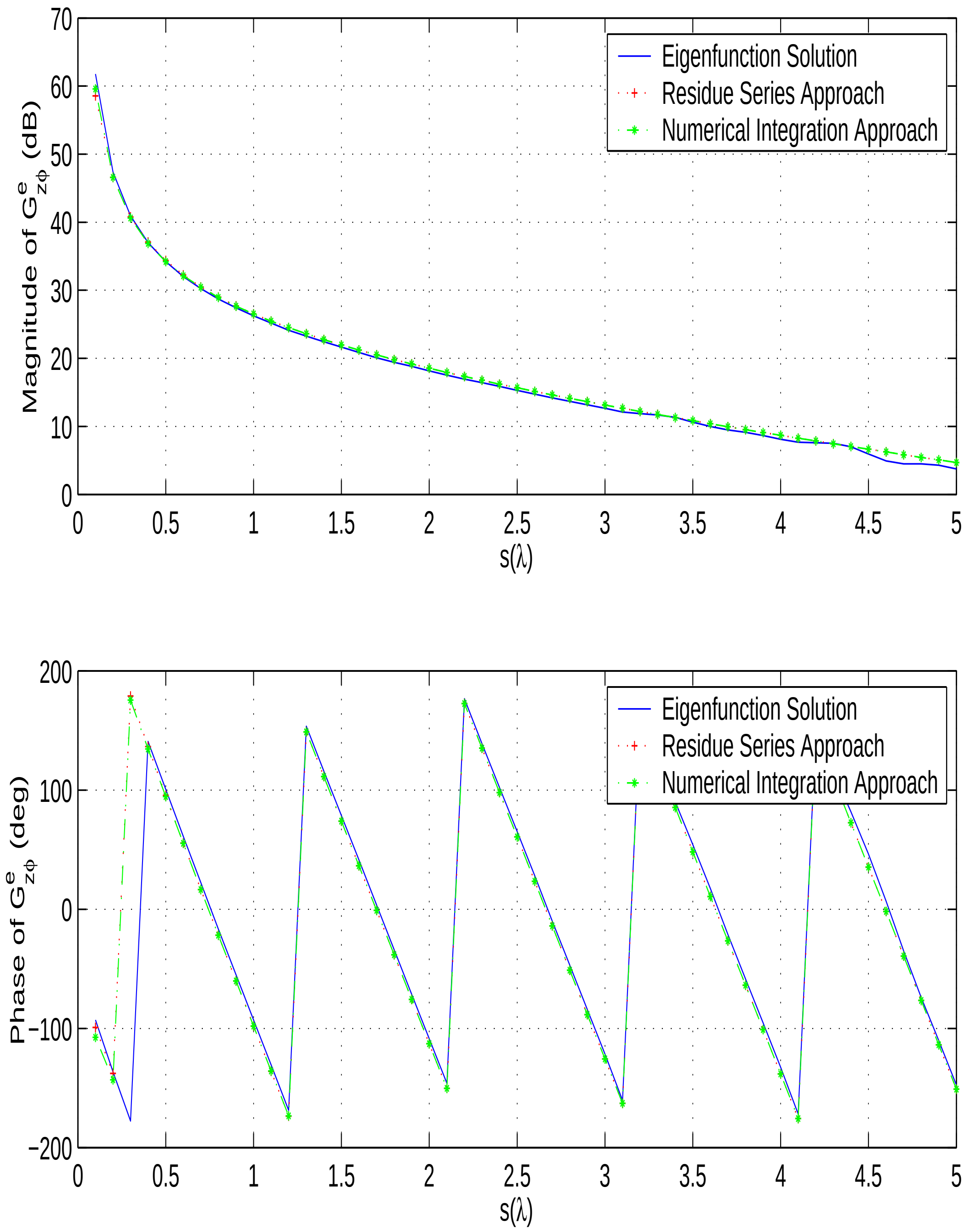

Figure 4.6: Comparison of the magnitude (in dB) and phase of the $G^e_{z\phi}$ versus separation, s, obtained by the eigenfunction solution and the numerical approaches for $f = 7GHz$, $a = 5\lambda$, $\alpha = 45°$ and $\Lambda = 0.1$.

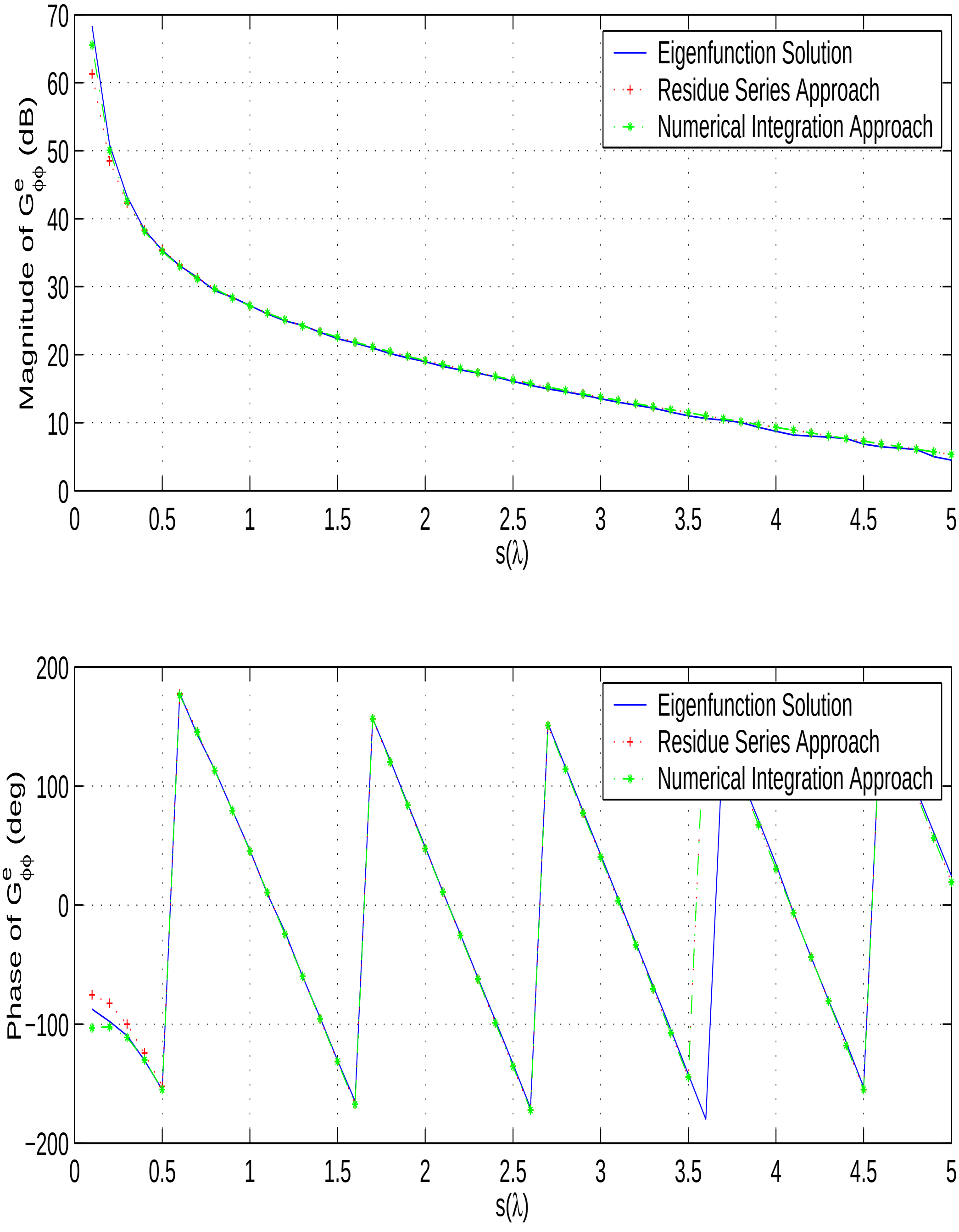

Figure 4.7: Comparison of the magnitude (in dB) and phase of the $G^e_{\phi\phi}$ versus separation, s, obtained by the eigenfunction solution and the numerical approaches for $f = 7GHz$, $a = 5\lambda$, $\alpha = 45°$ and $\Lambda = 0.1$.

disagreements between the eigenfunction solution and the two approaches are due to the convergence problem of the eigenfunction solution. In addition, the paraxial solution is very efficient in terms of the computational time since it is a closed-form solution.

Finally, various components of Green's function representations are computed for azimuthal angle (ϕ_d) varying from 0 to 45° at $f = 7\,GHz$ on the aforementioned cylinder (with a radius 5λ, and a normalized surface impedance $\Lambda = 0.1$) for a fixed $z_d = 3\lambda$. It is seen from the Fig. 4.9-4.11 that the UTD based solution is valid when $\phi_d > 20°$ (non-paraxial region of the cylinder) and paraxial solution is valid when $\phi_d < 25°$ (paraxial region of the cylinder). To have a complete solution, a transition point from the UTD based solution to the paraxial solution should be determined. In [14], it is suggested that the criterion for the transition point should be based on the Fock parameter, ξ,

$$\xi = (\frac{ka\cos\alpha}{2})^{1/3}\frac{s\cos\alpha}{a} \tag{4.1}$$

which depends on the radius of the cylinder, a, the path length, s, and the angle, α. Hence, the UTD based and the paraxial solutions can be employed for $\xi \geq 0.75$, and $\xi < 0.75$, respectively, to yield accurate results for the Green's function representations pertaining to various source and field orientations [14].

Consequently, the UTD based solution, evaluated with the numerical integration approach, and the closed-form paraxial solution form a complete and efficient solution for the Green's function representations pertaining the surface magnetic field on an electrically large circular cylinder with an IBC.

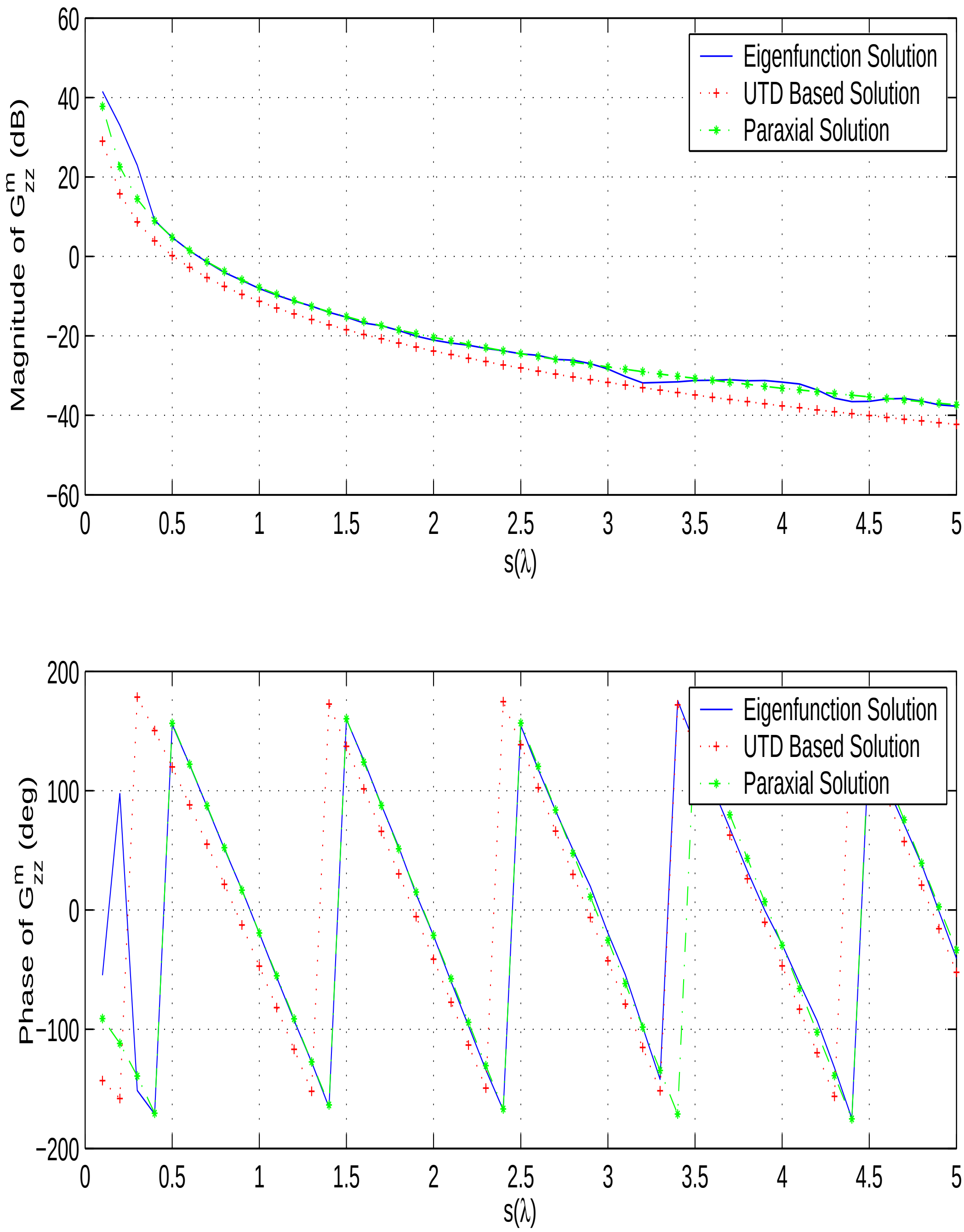

Figure 4.8: Comparison of the magnitude (in dB) and phase of the G^m_{zz} versus separation, s, obtained by the eigenfunction solution, the UTD based and paraxial solutions for $f = 7GHz$, $a = 5\lambda$, $\alpha = 80^\circ$ and $\Lambda = 0.1$.

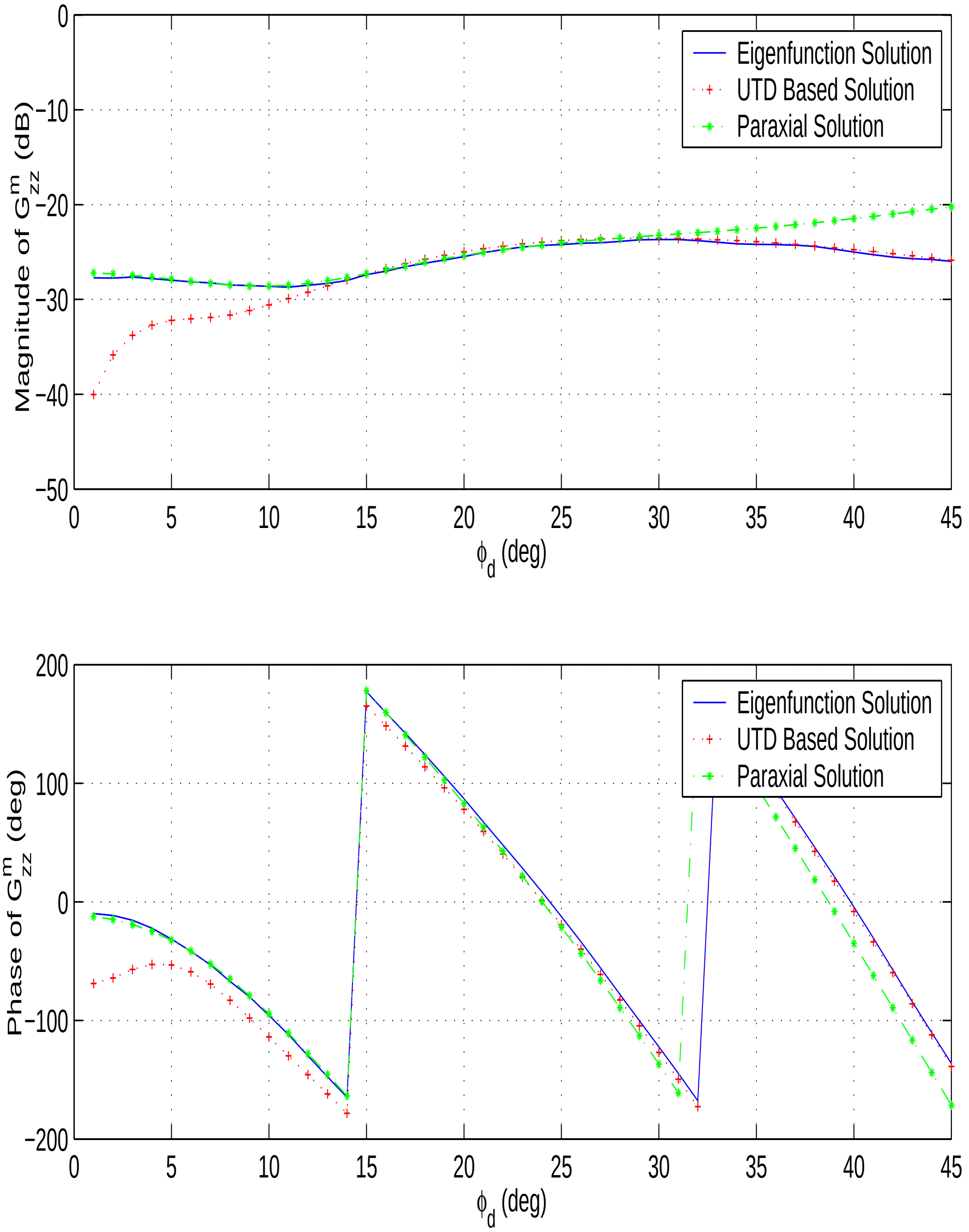

Figure 4.9: Comparison of the magnitude (in dB) and phase of the G^m_{zz} versus azimuthal angle, ϕ_d, obtained by the eigenfunction solution and the UTD based (evaluated by the numerical integration approach) and paraxial solutions for $f = 7GHz$, $a = 5\lambda$, $z_d = 3\lambda$ and $\Lambda = 0.1$.

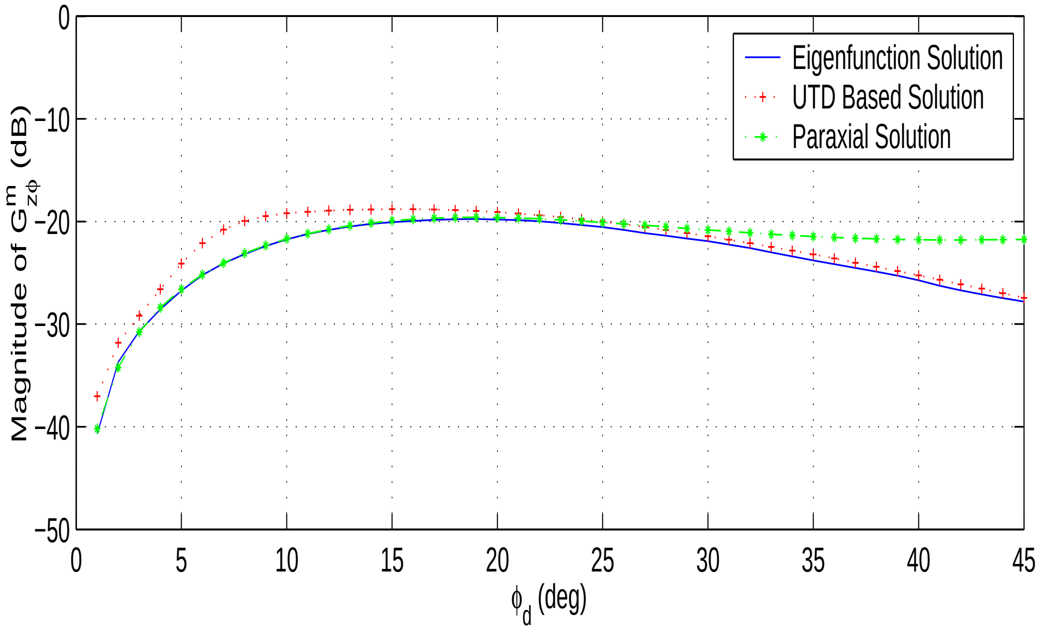

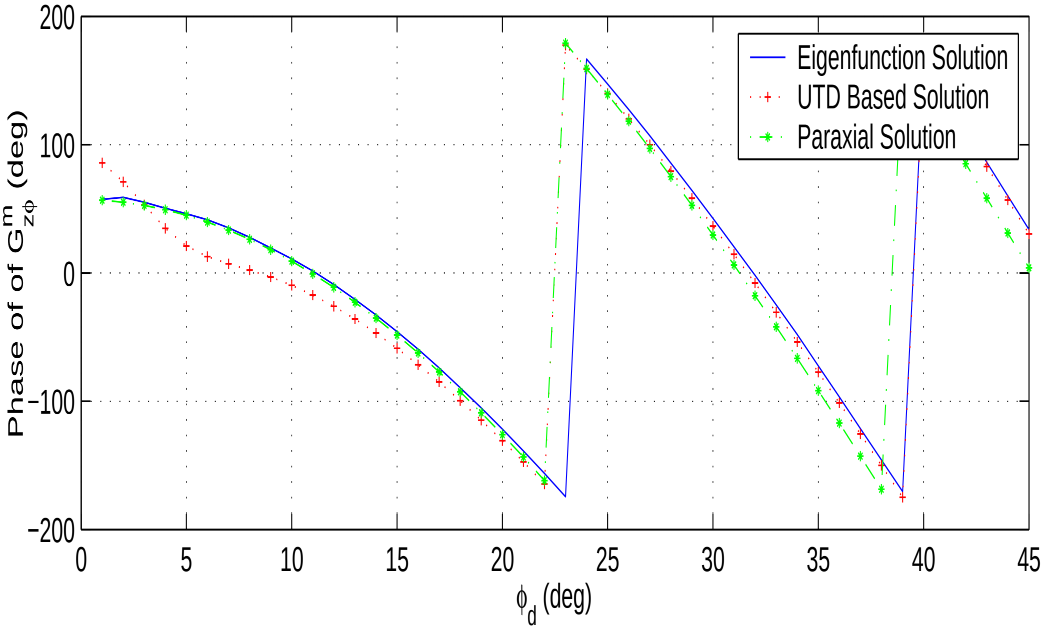

Figure 4.10: Comparison of the magnitude (in dB) and phase of the $G^m_{z\phi}$ versus azimuthal angle, ϕ_d, obtained by the eigenfunction solution and the UTD based (evaluated by the numerical integration approach) and paraxial solutions for $f = 7GHz$, $a = 5\lambda$, $z_d = 3\lambda$ and $\Lambda = 0.1$.

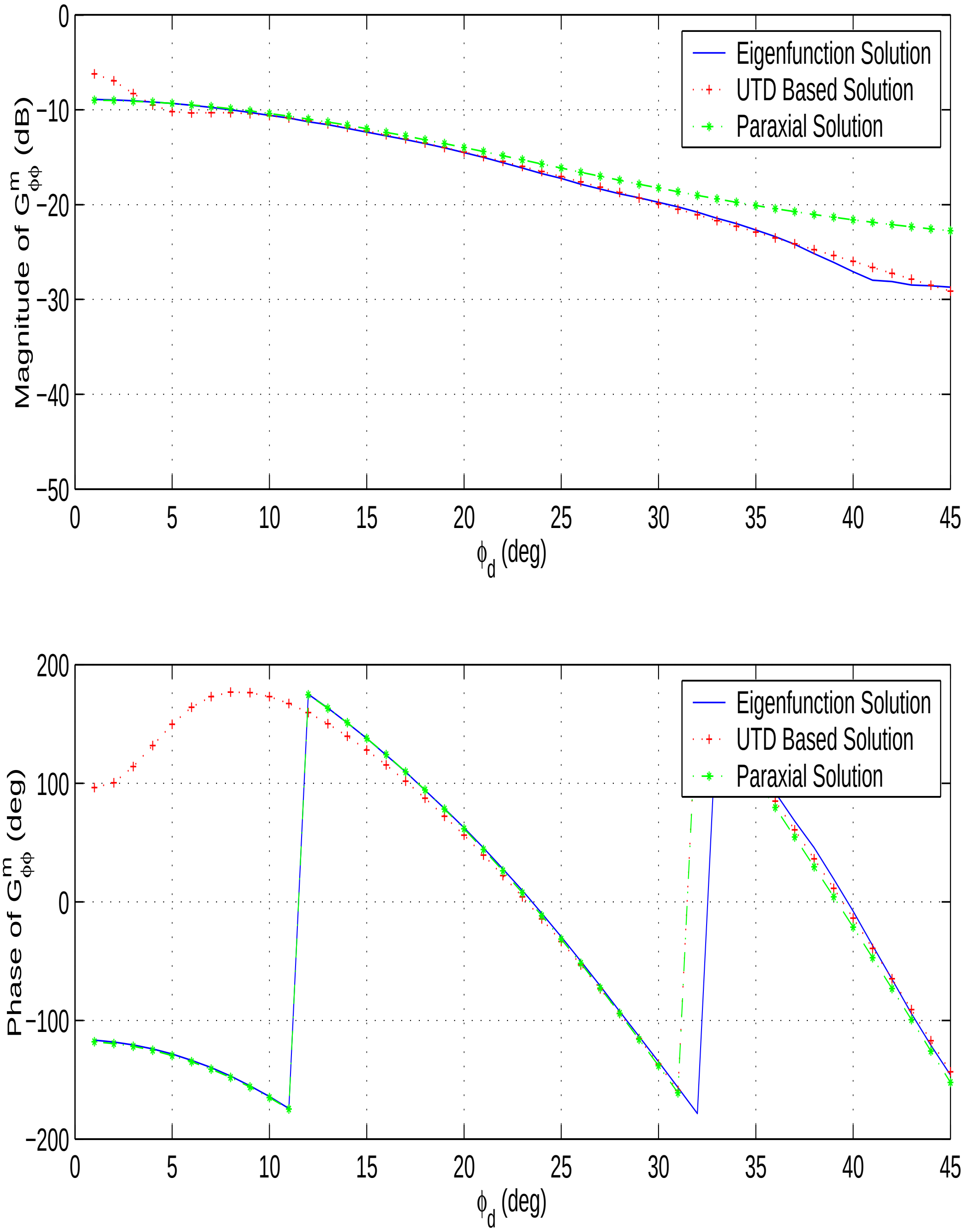

Figure 4.11: Comparison of the magnitude (in dB) and phase of the $G^m_{\phi\phi}$ versus azimuthal angle, ϕ_d, obtained by the eigenfunction solution and the UTD based (evaluated by the numerical integration approach) and paraxial solutions for $f = 7GHz$, $a = 5\lambda$, $z_d = 3\lambda$ and $\Lambda = 0.1$.

Chapter 5

Conclusions

Efficient computation of surface fields excited on an electrically large circular cylinder with an IBC is presented. Two different asymptotic solutions, which are called the UTD based and the paraxial solutions, are developed previously. An alternative numerical approach is presented for the evaluation of the UTD based asymptotic solution for the non-paraxial surface fields excited by a magnetic or an electric source located on the surface of an electrically large circular cylinder with an IBC. This alternative approach is based on performing a numerical integration for the Fock type integrals on a deformed path, which is the major burden in the evaluation of the UTD solution. The accuracy and efficiency of this approach is compared with the previously developed one presented in [14], which is based on invoking the Cauchy's residue theorem by finding the pole singularities numerically. Both approaches yield accurate results as they are compared with the eigenfunction solution in [14]. However, performing a numerical integration on the deformed path has several advantages over the Residue Series approach such as having an easier formulation and less computational time. Having these advantages makes the Numerical Integration approach more appealing than the Residue Series approach for the evaluation of the UTD based asymptotic solution for the surface fields excited on an electrically large circular cylinder with an IBC. In regard to paraxial surface fields, the paraxial solution is a closed-form solution, and very efficient in terms of the computational time. Hence, there is no need for an alternative approach for the evaluation of the non-paraxial surface fields.

As a result, the UTD based solution, evaluated with the numerical integration approach, and closed-form paraxial solution form a complete and efficient solution for the Green's function representations pertaining to the surface magnetic field on an electrically large circular cylinder with an IBC.

Appendix A

Derivation of (E_z, H_z) due to a Tangential Electric Source on a Circular Cylinder with an IBC

The electric and magnetic fields, $\vec{E}$ and $\vec{H}$, due to a point electric current satisfy the following vector wave equations

$$(\vec{\nabla}^2 + k^2)\begin{bmatrix} \vec{E}(\vec{r}) \\ \vec{H}(\vec{r}) \end{bmatrix} = \frac{jZ_0}{k}\begin{bmatrix} k^2 + \vec{\nabla}\vec{\nabla}\cdot \\ jk/Z_0\vec{\nabla}\times \end{bmatrix}\vec{J}(\vec{r}) \qquad \text{(A.1)}$$

where k is the free space wave number, Z_0 is the intrinsic impedance of free space, $\vec{r}'$ and $\vec{r}$ are the position vectors for the source and observation points, respectively, and the tangential electric current, $\vec{J}$, on the surface of the cylinder is given by

$$\vec{J}(\vec{r}) = (P_e^z\hat{z} + P_e^\phi\hat{\phi})\delta(\vec{r} - \vec{r}'). \qquad \text{(A.2)}$$

The $\hat{z}$ components of the electric and magnetic field correspond to the following equations:

$$(\vec{\nabla}^2 + k^2)\begin{bmatrix} E_z \\ H_z \end{bmatrix} = \frac{jZ_0}{k}\hat{z}\cdot\begin{bmatrix} k^2 + \vec{\nabla}\vec{\nabla}\cdot \\ jk/Z_0\vec{\nabla}\times \end{bmatrix}\vec{J}(\vec{r}). \qquad \text{(A.3)}$$

In an unbounded medium, E_z and H_z can be expressed as follows:

$$\begin{bmatrix} E_z \\ H_z \end{bmatrix} = -\frac{jZ_0}{k}\hat{z}\cdot\begin{bmatrix} k^2+\vec{\nabla}\vec{\nabla}\cdot \\ jk/Z_0\vec{\nabla}\times \end{bmatrix}(P_e^z\hat{z}+P_e^\phi\hat{\phi})\frac{e^{-jk|\vec{r}-\vec{r}'|}}{4\pi|\vec{r}-\vec{r}'|}. \tag{A.4}$$

The equations above can be modified to express electric and magnetic field in the terms of source point coordinates such that

$$\begin{bmatrix} E_z \\ H_z \end{bmatrix} = -\frac{jZ_0}{k}\hat{z}\cdot\begin{bmatrix} k^2+\vec{\nabla}'\vec{\nabla}'\cdot \\ -jk/Z_0\vec{\nabla}'\times \end{bmatrix}(P_e^z\hat{z}+P_e^\phi\hat{\phi})\frac{e^{-jk|\vec{r}-\vec{r}'|}}{4\pi|\vec{r}-\vec{r}'|}. \tag{A.5}$$

We expand the spherical wave as a spectral integral of a product of a cylindrical and plane waves using the Sommerfeld identity

$$\frac{e^{-jk|\vec{r}-\vec{r}'|}}{|\vec{r}-\vec{r}'|} = -\frac{j}{2}\int_{-\infty}^{\infty} dk_z e^{-jk_z z_d} H_0^{(2)}(k_\rho|\vec{\rho}-\vec{\rho}'|). \tag{A.6}$$

Using the Addition theorem, Hankel function can be expanded as an infinite summation of standing and outgoing waves as

$$H_0^{(2)}(k_\rho|\vec{\rho}-\vec{\rho}'|) = \sum_{n=-\infty}^{\infty} e^{jn\phi_d} J_n(k_\rho\rho_<)H_n^{(2)}(k_\rho\rho_>). \tag{A.7}$$

Now, $\hat{z}$ components of the electric and magnetic field can be expressed as

$$\begin{aligned}\begin{bmatrix} E_z \\ H_z \end{bmatrix} &= -\frac{Z_0}{8\pi k}\hat{z}\cdot\begin{bmatrix} k^2+\vec{\nabla}'\vec{\nabla}'\cdot \\ -jk/Z_0\vec{\nabla}'\times \end{bmatrix}(P_e^z\hat{z}+P_e^\phi\hat{\phi})\int_{-\infty}^{\infty} dk_z e^{-jk_z z_d} \\ &\qquad H_0^{(2)}(k_\rho|\vec{\rho}-\vec{\rho}'|)\sum_{n=-\infty}^{\infty} e^{jn\phi_d} J_n(k_\rho\rho_<)H_n^{(2)}(k_\rho\rho_>).\end{aligned} \tag{A.8}$$

The orders of the derivatives and integral can be interchanged to yield

$$\begin{bmatrix} E_z \\ H_z \end{bmatrix} = -\frac{1}{2\pi}\int_{-\infty}^{\infty} dk_z e^{-jk_z z_d}\sum_{n=-\infty}^{\infty} e^{jn\phi_d} J_n(k_\rho\rho_<)H_n^{(2)}(k_\rho\rho_>)\overleftarrow{S} \tag{A.9}$$

where the operator $\overleftarrow{S}$, which acts on functions to its left and is defined for the $e^{-jk_z z'-jn\phi'}$ dependence [27], is given by

$$\overleftarrow{S} = -\frac{1}{4k\rho'}\begin{bmatrix} Z_0(k_\rho^2\rho' P_e^z + nk_z P_e^\phi) \\ -jk_{\rho'}P_e^\phi\partial/\partial\rho' \end{bmatrix}. \tag{A.10}$$

If we introduce a circular cylinder into the unbounded medium, such that $\rho' > a$ and $\rho > a$, taking the reflections from the cylinder into account field components can be written as

$$\begin{bmatrix} E_z \\ H_z \end{bmatrix} = -\frac{1}{2\pi}\int_{-\infty}^{\infty} dk_z e^{-jk_z z_d} \sum_{n=-\infty}^{\infty} e^{jn\phi_d} \begin{bmatrix} \tilde{E}_{z_n} \\ \tilde{H}_{z_n} \end{bmatrix} \tag{A.11}$$

where $\tilde{E}_{z_n}$ and $\tilde{H}_{z_n}$ are the n^{th} harmonics of E_z and H_z, respectively, such that

$$\begin{bmatrix} \tilde{E}_{z_n} \\ \tilde{H}_{z_n} \end{bmatrix} = \begin{cases} [J_n(k_\rho\rho)\bar{I} + H_n^{(2)}(k_\rho\rho)\bar{R}]H_n^{(2)}(k_\rho\rho')\overleftarrow{S}, & \rho < \rho' \\ H_n^{(2)}(k_\rho\rho)[J_n(k_\rho\rho')\bar{I} + H_n^{(2)}(k_\rho\rho')\bar{R}]\overleftarrow{S}, & \rho > \rho' \end{cases} \tag{A.12}$$

where $\bar{I}$ and $\bar{R}$ are identity and reflection matrices, respectively.

Using the Maxwell's equations, E_ϕ and H_ϕ can be written in terms of E_z and H_z such that

$$(k^2 + \frac{\partial^2}{\partial z^2})\begin{bmatrix} H_\phi \\ E_\phi \end{bmatrix} = \frac{1}{\rho}\begin{bmatrix} -jZ_0^{-1}k\rho\partial/\partial\rho & \partial^2/\partial z\partial\phi \\ \partial^2/\partial z\partial\phi & jZ_0k\rho\partial/\partial\rho \end{bmatrix}\begin{bmatrix} E_z \\ H_z \end{bmatrix} \tag{A.13}$$

in which the n^{th} harmonics of E_ϕ and H_ϕ, $\tilde{E}_{\phi_n}$ and $\tilde{H}_{\phi_n}$ are related to $\tilde{E}_{z_n}$ and $\tilde{H}_{z_n}$ as follows:

$$\begin{bmatrix} \tilde{H}_{\phi_n} \\ \tilde{E}_{\phi_n} \end{bmatrix} = \frac{1}{k_\rho^2\rho}\begin{bmatrix} -jZ_0^{-1}k\rho\partial/\partial\rho & nk_z \\ nk_z & jZ_0k\rho\partial/\partial\rho \end{bmatrix}\begin{bmatrix} \tilde{E}_{z_n} \\ \tilde{H}_{z_n} \end{bmatrix}. \tag{A.14}$$

Thus, $\hat{\phi}$ components of the electric and magnetic fields, E_ϕ and H_ϕ, can be expressed as

$$\begin{bmatrix} H_\phi \\ E_\phi \end{bmatrix} = -\frac{1}{2\pi}\int_{-\infty}^{\infty} dk_z e^{-jk_z z_d} \sum_{n=-\infty}^{\infty} e^{jn\phi_d} \begin{bmatrix} \tilde{H}_{\phi_n} \\ \tilde{E}_{\phi_n} \end{bmatrix} \tag{A.15}$$

such that

$$\begin{bmatrix} \tilde{H}_{\phi_n} \\ \tilde{E}_{\phi_n} \end{bmatrix} = \begin{cases} [\bar{J}_n(k_\rho\rho)\bar{I} + \bar{H}_n^{(2)}(k_\rho\rho)\bar{R}]H_n^{(2)}(k_\rho\rho')\overleftarrow{S}, & \rho < \rho' \\ \bar{H}_n^{(2)}(k_\rho\rho)[J_n(k_\rho\rho')\bar{I} + H_n^{(2)}(k_\rho\rho')\bar{R}]\overleftarrow{S}, & \rho > \rho' \end{cases} \tag{A.16}$$

in which

$$\bar{B}_n(k_\rho\rho) = \frac{1}{k_\rho^2\rho}\begin{bmatrix} -jZ_0^{-1}kk_\rho\rho B_n'(k_\rho\rho) & nk_zB_n(k_\rho\rho) \\ nk_zB_n(k_\rho\rho) & jZ_0kk_\rho\rho B_n'(k_\rho\rho) \end{bmatrix} \tag{A.17}$$

where B_n is either J_n or $H_n^{(2)}$ depending on whether $\bar{J}_n$ or $\bar{H}_n^{(2)}$ is evaluated, respectively.

The tangential components of the fields have to satisfy the following IBC [28]

$$\left.\begin{bmatrix} E_z \\ H_z \end{bmatrix}\right|_{\rho=a} = \bar{Z}_s \left.\begin{bmatrix} H_\phi \\ E_\phi \end{bmatrix}\right|_{\rho=a} \tag{A.18}$$

on the surface of the cylinder with

$$\bar{Z}_s = \begin{bmatrix} Z_s & 0 \\ 0 & -Z_s^{-1} \end{bmatrix}. \tag{A.19}$$

Since the source is not on the cylinder yet, the expressions for $\rho < \rho'$ in (A.12) and (A.16) are inserted in the IBC for the n^{th} harmonics

$$\left.\begin{bmatrix} \tilde{E}_{z_n} \\ \tilde{H}_{z_n} \end{bmatrix}\right|_{\rho=a} = \bar{Z}_z \left.\begin{bmatrix} \tilde{H}_{\phi_n} \\ \tilde{E}_{\phi_n} \end{bmatrix}\right|_{\rho=a} \tag{A.20}$$

to obtain the reflection matrix

$$\bar{R} = -[H_n^{(2)}(k_\rho a)\bar{I} - \bar{Z}_s \bar{H}_n^{(2)}(k_\rho a)]^{-1}[J_n(k_\rho a)\bar{I} - \bar{Z}_s \bar{J}_n(k_\rho a)]. \tag{A.21}$$

The reflection matrix can be written as

$$\bar{R} = -\frac{1}{H_n^{(2)}(k_\rho a) D_c} \begin{bmatrix} R_{11} & R_{12} \\ R_{21} & R_{22} \end{bmatrix} \tag{A.22}$$

where

$$R_{11} = J_n(k_\rho a)[N_{\phi\phi} + N_{z\phi}^2] + J_n'(k_\rho a)\frac{[N_{\phi\phi}(N_{zz} - 1)]}{R_n} \tag{A.23}$$

$$R_{12} = j\frac{kZ_0}{k_\rho} N_{z\phi}[J_n'(k_\rho a) - J_n(k_\rho a)R_n] \tag{A.24}$$

$$R_{21} = -j\frac{k}{k_\rho Z_0} N_{z\phi}[J_n'(k_\rho a) - J_n(k_\rho a)R_n] \tag{A.25}$$

$$R_{22} = J_n(k_\rho a)[N_{zz} + N_{z\phi}^2] + J_n'(k_\rho a)\frac{[N_{zz}(N_{\phi\phi} - 1)]}{R_n} \tag{A.26}$$

$$D_c = N_{zz}N_{\phi\phi} + N_{z\phi}^2 \tag{A.27}$$

with

$$
\begin{aligned}
N_{zz} &= 1 + j\frac{k}{k_\rho}\Lambda R_n &\text{(A.28)}\\
N_{z\phi} &= \frac{nk_z}{k_\rho^2 a} &\text{(A.29)}\\
N_{\phi\phi} &= 1 + j\frac{k}{k_\rho}\Lambda^{-1} R_n &\text{(A.30)}
\end{aligned}
$$

$$
R_n = \frac{H_n^{(2)'}(k_\rho a)}{H_n^{(2)}(k_\rho a)}. \tag{A.31}
$$

Inserting (A.22) into (A.11) for $\rho > \rho'$ and setting $\rho' = a$ (source is placed on the cylinder) yield

$$
\begin{bmatrix} \tilde{E}_{z_n} \\ \tilde{H}_{z_n} \end{bmatrix} = H_n^{(2)}(k_\rho \rho)
$$

$$
\begin{bmatrix} J_n(k_\rho\rho) - \frac{H_n^{(2)}(k_\rho\rho')}{H_n^{(2)}(k_\rho a)} R_{11} D_c & -\frac{H_n^{(2)}(k_\rho\rho')}{H_n^{(2)}(k_\rho a)} R_{12} D_c \\ -\frac{H_n^{(2)}(k_\rho\rho')}{H_n^{(2)}(k_\rho a)} R_{21} D_c & J_n(k_\rho\rho) - \frac{H_n^{(2)}(k_\rho\rho')}{H_n^{(2)}(k_\rho a)} R_{22} D_c \end{bmatrix} \cdot \overleftarrow{S}\Big|_{\rho'=a} \tag{A.32}
$$

Then, the n^{th} harmonics of E_z and H_z can be expressed as

$$
\begin{aligned}
\tilde{E}_{z_n} &= -\frac{H_n^{(2)}(k_\rho\rho)}{4k\rho'}\Bigg[\hat{\phi}P_e^\phi(nk_z Z_0(J_n(k_\rho\rho) - \frac{H_n^{(2)}(k_\rho\rho')R_{11}}{H_n^{(2)}(k_\rho a)}D_c) + jk\rho'\frac{\partial}{\partial\rho'} \\
&\quad (-\frac{H_n^{(2)}(k_\rho\rho')R_{12}}{H_n^{(2)}(k_\rho a)}D_c) + \hat{z}P_e^z k_\rho^2 Z_0(J_n(k_\rho\rho) - \frac{H_n^{(2)}(k_\rho\rho')R_{11}}{H_n^{(2)}(k_\rho a)}D_c)\Bigg]\Bigg|_{\rho'=a} &\text{(A.33)}\\
\tilde{H}_{z_n} &= -\frac{H_n^{(2)}(k_\rho\rho)}{4k\rho'}\Bigg[\hat{\phi}P_e^\phi(nk_z Z_0(-\frac{H_n^{(2)}(k_\rho\rho')R_{21}}{H_n^{(2)}(k_\rho a)}D_c)jk\rho'\frac{\partial}{\partial\rho'}(J_n(k_\rho\rho) - \\
&\quad \frac{H_n^{(2)}(k_\rho\rho')R_{22}}{H_n^{(2)}(k_\rho a)}D_c) + \hat{z}P_e^z k_\rho^2 Z_0(-\frac{H_n^{(2)}(k_\rho\rho')R_{21}}{H_n^{(2)}(k_\rho a)}D_c)\Bigg]\Bigg|_{\rho'=a}. &\text{(A.34)}
\end{aligned}
$$

Finally, $\hat{z}$ components of the electric and magnetic fields due to the tangential electric source given by (A.2) are obtained as

$$
\begin{aligned}
E_z &= -\frac{Z_s}{4\pi^2 a}\int_{-\infty}^{\infty} dk_z e^{-jk_z z_d} \sum_{n=-\infty}^{\infty} \frac{e^{jn\phi_d}}{D_c}[(1+\frac{j\Lambda^{-1}k}{k_\rho}R_n)P_e^z + \frac{nk_z}{k_\rho^2 a}P_e^\phi] \\
&\quad \frac{H_n^{(2)}(k_\rho \rho)}{H_n^{(2)}(k_\rho a)} \qquad \text{(A.35)} \\
H_z &= \frac{1}{4\pi^2 a}\int_{-\infty}^{\infty} dk_z e^{-jk_z z_d} \sum_{n=-\infty}^{\infty} \frac{e^{jn\phi_d}}{D_c}[\frac{nk_z}{k_\rho^2 a}P_e^z + (1+\frac{j\Lambda k}{k_\rho}R_n)P_e^\phi] \\
&\quad \frac{H_n^{(2)}(k_\rho \rho)}{H_n^{(2)}(k_\rho a)}. \qquad \text{(A.36)}
\end{aligned}
$$

Appendix B

The Procedure for the Development of High Frequency Solutions for Electric Source Excitation

The tangential surface field excited by a tangential electric source can be derived for the geometry given in Fig. 2.2 using a formulation similar to the procedure presented in [14]. Firstly, $\hat{z}$ components of electric and magnetic fields due to a tangential electric source

$$\vec{P}_e = P_e^z \hat{z} + P_e^\phi \hat{\phi} \tag{B.1}$$

located on the surface is derived in Appendix A as

$$\begin{aligned} E_z &= -\frac{Z_s}{4\pi^2 a} \int_{-\infty}^{\infty} dk_z e^{-jk_z z_d} \sum_{n=-\infty}^{\infty} \frac{e^{jn\phi_d}}{D_c} [(1 + \frac{j\Lambda^{-1}k}{k_\rho} R_n) P_e^z + \frac{nk_z}{k_\rho^2 a} P_e^\phi] \\ & \quad \frac{H_n^{(2)}(k_\rho \rho)}{H_n^{(2)}(k_\rho a)} \qquad (B.2) \\ H_z &= \frac{1}{4\pi^2 a} \int_{-\infty}^{\infty} dk_z e^{-jk_z z_d} \sum_{n=-\infty}^{\infty} \frac{e^{jn\phi_d}}{D_c} [\frac{nk_z}{k_\rho^2 a} P_e^z + (1 + \frac{j\Lambda k}{k_\rho} R_n) P_e^\phi] \\ & \quad \frac{H_n^{(2)}(k_\rho \rho)}{H_n^{(2)}(k_\rho a)}. \qquad (B.3) \end{aligned}$$

Once the $\hat{z}$ components of the fields (E_z, H_z) are obtained, the vector potentials (A_z, F_z) due to these components can easily be found using the methods described in [20]. Then, the procedure explained in [14] is followed. Namely, first Watson transform, which is expressed in Appendix C, is applied to the potentials to get

$$A_z = \sum_{\ell=0}^{\infty}(A^+_{z_\ell} + A^-_{z_\ell}) \tag{B.4}$$

$$F_z = \sum_{\ell=0}^{\infty}(F^+_{z_\ell} + F^-_{z_\ell}) \tag{B.5}$$

where $A^+_{z_\ell}$, and $F^+_{z_\ell}$ pertains the surface waves propagating around the cylinder in the positive $\hat{\phi}$ direction, whereas $A^-_{z_\ell}$, and $F^-_{z_\ell}$ corresponds to those propagating in the negative $\hat{\phi}$ direction.

Thereby the potentials are expressed as double integrals over the axial (k_z) and the azimuthal (ν) wavenumbers such that

$$\begin{aligned} A^\pm_{z_\ell} &= \frac{j\Lambda}{4\pi^2 ak}\int_{-\infty}^{\infty} dk_z e^{-jk_z z_d}\int_{-\infty}^{\infty} d\nu e^{-j\nu\phi^\pm_\ell}\frac{1}{D_\nu} \\ &\quad [(1+\frac{j\Lambda^{-1}k}{k_\rho}R_\nu)P^z_e \mp \frac{\nu k_z}{k_\rho^2 a}P^\phi_e]\frac{H^{(2)}_\nu(k_\rho\rho)}{H^{(2)}_\nu(k_\rho a)} \end{aligned} \tag{B.6}$$

$$\begin{aligned} F^\pm_{z_\ell} &= \frac{jZ_0}{4\pi^2 ak}\int_{-\infty}^{\infty} dk_z e^{-jk_z z_d}\int_{-\infty}^{\infty} d\nu e^{-j\nu\phi^\pm_\ell}\frac{1}{D_\nu} \\ &\quad (\pm\frac{\nu k_z}{k_\rho^2 a}P^z_e + (1+\frac{j\Lambda k}{k_\rho}R_\nu)P^\phi_e]\frac{H^{(2)}_\nu(k_\rho\rho)}{H^{(2)}_\nu(k_\rho a)} \end{aligned} \tag{B.7}$$

where

$$D_\nu = (R_\nu - \frac{j\Lambda k_\rho}{k})(R_\nu - \frac{j\Lambda^{-1}k_\rho}{k}) - (\frac{\nu k_z}{kk_\rho a})^2 \tag{B.8}$$

$$R_\nu = \frac{H^{(2)'}_\nu(k_\rho a)}{H^{(2)}_\nu(k_\rho a)}. \tag{B.9}$$

Employing a Fock-substitution $(\nu = k_\rho a + m_t\tau)$, integration in the ν-plane is replaced by integration in the τ-plane as follows:

$$\begin{aligned}
A_{z_\ell}^{\pm} &= \frac{j\Lambda}{4\pi^2 ak}\int_{-\infty}^{\infty} dk_z e^{-j(k_z z_d + k_\rho a\phi_\ell^{\pm})}\int_{-\infty}^{\infty} d\tau e^{-j\xi\tau}\frac{m_t}{D_\nu} \\
&\quad [(1+\frac{j\Lambda^{-1}k}{k_\rho}R_\nu)P_e^z \mp \frac{k_z}{k_\rho}(1+\frac{\tau}{2m_t^2})P_e^\phi]\frac{H_\nu^{(2)}(k_\rho\rho)}{H_\nu^{(2)}(k_\rho a)} \qquad \text{(B.10)} \\
F_{z_\ell}^{\pm} &= \frac{jZ_0}{4\pi^2 ak}\int_{-\infty}^{\infty} dk_z e^{-j(k_z z_d + k_\rho a\phi_\ell^{\pm})}\int_{-\infty}^{\infty} d\tau e^{-j\xi\tau}\frac{m_t}{D_\nu} \\
&\quad (\pm\frac{k_z}{k_\rho}(1+\frac{\tau}{2m_t^2})P_e^z + (1+\frac{j\Lambda k}{k_\rho}R_\nu)P_e^\phi]\frac{H_\nu^{(2)}(k_\rho\rho)}{H_\nu^{(2)}(k_\rho a)}. \qquad \text{(B.11)}
\end{aligned}$$

Below, relevant vector potential expressions to find the surface magnetic field are given

$$\begin{aligned}
\left.\frac{\partial A_{z_\ell}^{\pm}}{\partial\rho}\right|_{\rho=a} &= \frac{j\Lambda}{4\pi^2 a}\int_{C_\psi} d\psi e^{-jks\cos(\psi-\alpha)}\int_{-\infty}^{\infty} d\tau e^{-j\xi\tau}\frac{m_t}{D_\nu} \\
&\quad \cos\psi[(\cos\psi + j\Lambda^{-1}R_\nu)P_e^z \mp \sin\psi(1+\frac{\tau}{2m_t^2})P_e^\phi]R_\nu \qquad \text{(B.12)} \\
\left.F_{z_\ell}^{\pm}\right|_{\rho=a} &= \frac{jZ_0}{4\pi^2 a}\int_{C_\psi} d\psi e^{-jks\cos(\psi-\alpha)}\int_{-\infty}^{\infty} d\tau e^{-j\xi\tau}\frac{m_t}{D_\nu} \\
&\quad [\pm\sin\psi(1+\frac{\tau}{2m_t^2})P_e^z + (\cos\psi + j\Lambda R_\nu)P_e^\phi] \qquad \text{(B.13)}
\end{aligned}$$

which are evaluated on the surface of cylinder ($\rho = a$).

Then, introducing a standard polar transformation along with some geometrical relations, integration over k_z is converted to a complex contour integral which is evaluated applying the method of steepest descent, which is expressed in Appendix D, assuming that the separation s between the source and field points is the large parameter, resulting

$$\begin{aligned}
\left.\frac{\partial A_{z_\ell}^{\pm}}{\partial\rho}\right|_{\rho=a} &\sim \frac{j\Lambda k}{2\pi}\frac{e^{-jks}}{s}\cos\alpha\sqrt{\frac{j\xi}{4\pi}}\int_{-\infty}^{\infty} d\tau e^{-j\xi\tau}\frac{1}{m_t D_\nu} \\
&\quad [(\cos\alpha + j\Lambda^{-1}R_\nu)P_e^z \mp \sin\alpha(1+\frac{\tau}{2m_t^2})P_e^\phi]R_\nu \qquad \text{(B.14)} \\
\left.F_{z_\ell}^{\pm}\right|_{\rho=a} &\sim \frac{jZ_0}{2\pi}\frac{e^{-jks}}{s}\sqrt{\frac{j\xi}{4\pi}}\int_{-\infty}^{\infty} d\tau e^{-j\xi\tau}\frac{1}{m_t D_\nu} \\
&\quad [\pm\sin\alpha(1+\frac{\tau}{2m_t^2})P_e^z + (\cos\alpha + j\Lambda R_\nu)P_e^\phi]. \qquad \text{(B.15)}
\end{aligned}$$

Finally, the field expressions are obtained by performing the derivatives to the resultant potential expressions analytically (where the terms including higher powers of m_t^{-2} are neglected) using the following tangential surface magnetic field expression:

$$\vec{H}_{t_\ell}^{\pm} = -\frac{j}{kZ_0}[\hat{z}(\frac{\partial^2}{\partial z_d^2} + k^2)F_{z_\ell}^{\pm} + \hat{\phi}(\pm\frac{a}{\rho}\frac{\partial^2 F_{z_\ell}^{\pm}}{\partial y_\ell \partial z_d} - jZ_0 k\frac{\partial A_{z_\ell}^{\pm}}{\partial \rho})]\bigg|_{\rho=a}. \tag{B.16}$$

Appendix C

Watson Transformation

This transformation converts an infinite summation into an integration by way of the following identity

$$\sum_{n=-\infty}^{\infty} e^{jn\phi_d} H(n) = \frac{j}{2} \oint_{C_+ + C_-} d\nu \frac{e^{-j\nu(\pi-\phi_d)}}{\sin(\nu\pi)} H(\nu) \tag{C.1}$$

which is a direct outcome of the Cauchy's residue theorem. Only the singularities associated with the zeros of $\sin(\nu\pi)$, which are at $\nu = 0, \pm 1, ..., \pm\infty$, are interior to the closed integration path, $C_+ + C_-$ as shown in Fig. C.1. The relation in (C.1) can be expressed explicitly as

$$\begin{aligned}
\sum_{n=-\infty}^{\infty} e^{jn\phi_d} H(n) &= \frac{j}{2} \left[\int_{-\infty+j\epsilon}^{\infty+j\epsilon} d\nu \frac{e^{-j\nu(\pi-\phi_d)}}{\sin(\nu\pi)} H(\nu) + \int_{\infty-j\epsilon}^{-\infty-j\epsilon} d\nu \frac{e^{-j\nu(\pi-\phi_d)}}{\sin(\nu\pi)} H(\nu) \right] \\
&= \frac{j}{2} \int_{-\infty+j\epsilon}^{\infty+j\epsilon} d\nu \frac{e^{j\nu(\pi-\phi_d)} H(-\nu) + e^{-j\nu(\pi-\phi_d)} H(\nu)}{\sin(\nu\pi)} \qquad \text{(C.2)}
\end{aligned}$$

where ϵ is real, positive and sufficiently small. Substituting the following identity

$$\begin{aligned}
\frac{1}{\sin(\nu\pi)} &= \frac{2j}{e^{j\nu\pi} - e^{-j\nu\pi}} \\
&= 2je^{-j\nu\pi} \frac{1}{1 - e^{-j\nu 2\pi}} \\
&= 2je^{-j\nu\pi} \sum_{\ell=0}^{\infty} e^{-j\nu 2\pi\ell} \qquad \text{(C.3)}
\end{aligned}$$

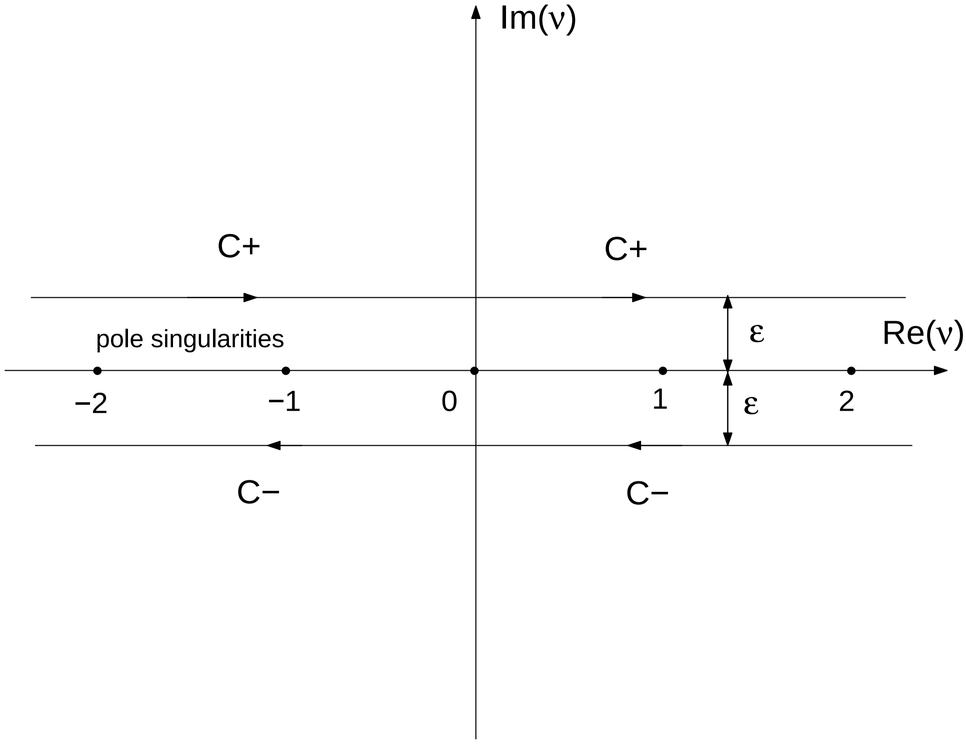

Figure C.1: Integration paths, C_+ and C_-, and pole singularities on the complex ν plane.

into C.2 and setting $\epsilon = 0$ yield

$$\sum_{n=-\infty}^{\infty} e^{jn\phi_d} H(n) = \int_{-\infty}^{\infty} d\nu \sum_{\ell=0}^{\infty} [e^{-j\nu\phi_\ell^+} H(-\nu) + e^{-j\nu\phi_\ell^-} H(\nu)] \tag{C.4}$$

where

$$\phi_\ell^{\pm} = \pm(\phi_d - \pi) + (2\ell + 1)\pi \qquad \ell = 0, 1, ..., \infty. \tag{C.5}$$

Appendix D

Method of Steepest Descent

In this method, integrals of the form

$$I(k) = \int_{C_\psi} e^{kf(\psi)} g(\psi) d\psi \tag{D.1}$$

are evaluated by localizing the dominant contribution to the integral to a small region of the integration contour. In (D.1), $f(\psi)$ and $g(\psi)$ are analytical complex valued functions, k is a large, positive real number, and $f(\psi)$ is slowly varying along the path of integration, C_ψ, which is shown in Fig D.1. Any point, ψ_s, where $f'(\psi_s) = 0$ and $f''(\psi_s) \neq 0$ (f' and f'' are the first and second derivative of f with respect to ψ respectively), is said to be the saddle point where the major contribution to the integral comes from the vicinity of this point. The path of integration can be deformed to go over the saddle point by the steepest possible route without changing the value of the integral as long as $g(\psi)$ does not have any singularities within the region which is swept during the deformation. Along this path, the integral becomes Gaussian and it can be evaluated as

$$I(k) \sim e^{j\theta} \sqrt{\frac{2\pi}{k|f''(\psi_s)|}} e^{kf(\psi_s)} g(\psi_s) \tag{D.2}$$

where θ is direction of the steepest descent.

In the derivation of the surface fields, the evaluation of integrals of the form

$$\int_{C_\psi} e^{-jks\cos(\psi-\alpha)} g(\psi) d\psi \tag{D.3}$$

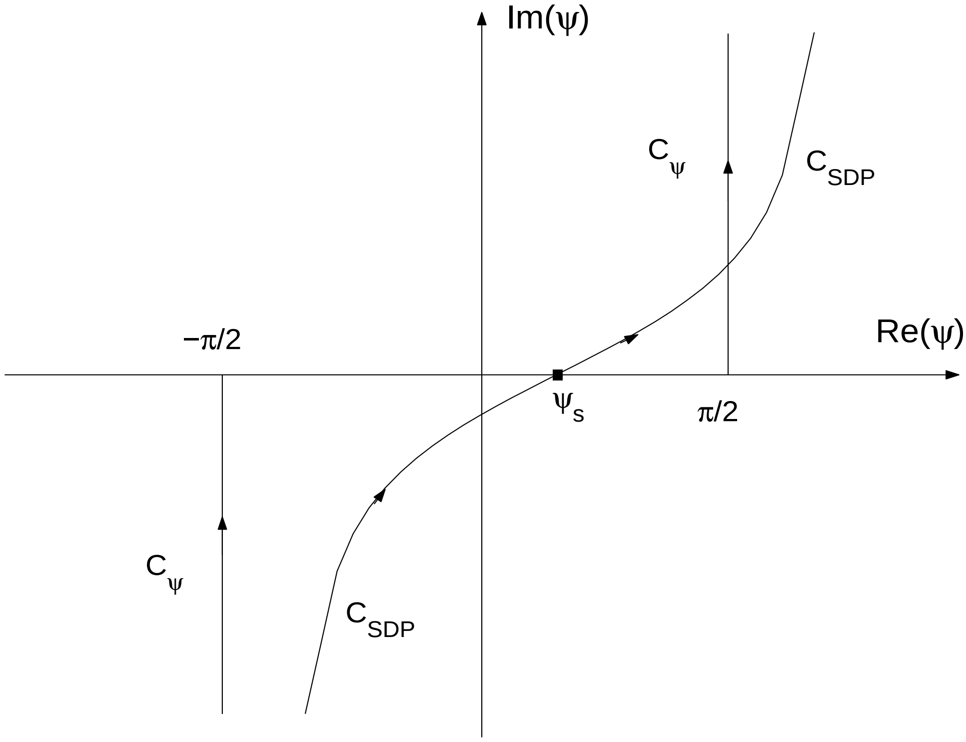

Figure D.1: Integration paths, C_ψ and C_{SDP}, on the complex ψ plane.

is required. In (D.3), $f(\psi) = -j\cos(\psi - \alpha)$. The saddle points are given by

$$f'(\psi) = j\sin(\psi - \alpha) \quad \Rightarrow \quad \sin(x - \alpha) = 0 \quad \Rightarrow \quad \psi_s = \alpha \pm n\pi. \tag{D.4}$$

From the given path C_ψ, we can deform onto a contour passing through the saddle point at $\psi_s = \alpha$. To find the steepest descent path, it is convenient to write $f(\psi)$ in real and imaginary parts. Letting $\psi = x + jy$, $f(\psi)$ can be expressed as

$$f(\psi) = -\sin(x - \alpha)\sinh(y) - j\cos(x - \alpha)\cosh(y). \tag{D.5}$$

Since the imaginary part $f(\psi)$ is constant along the steepest descent

$$Im[f(\psi)] = Im[f(\alpha)] \quad \Rightarrow \quad Im[-j\cos(x - \alpha)] = Im[-j] \tag{D.6}$$

the equation of the steepest descent/ascent contours is found to be

$$\cos(x - \alpha)\cosh(y) = 1. \tag{D.7}$$

In order to find the steepest descent contour, $f(\psi)$ is approximated to a quadratic order around $\psi = \alpha$ as

$$\begin{aligned} f(\psi) &\approx f(\alpha) + \frac{1}{2}(\psi - \alpha)^2 f''(\alpha) \\ &\approx -j + \frac{1}{2}(\psi - \alpha)^2 j. \end{aligned} \tag{D.8}$$

On the line of the steepest descent, $(\psi - \alpha)^2 j = -\lambda^2$ where λ is real. The solution to this equation is $\psi = \alpha + \lambda e^{j\pi/4}$, which means that the steepest descent makes an angle of $\pi/4$ with the positive x-axis. Thus, the integration path, C_ψ, can be deformed into the steepest descent path, C_{SDP}, which is shown in Fig D.1. Finally, local contribution from the saddle point is calculated to yield

$$\int_{C_\psi} e^{-jks\cos(\psi-\alpha)} g(\psi) d\psi \sim e^{j\pi/4} \sqrt{\frac{2\pi}{k}} e^{-jks} g(\alpha). \tag{D.9}$$

Bibliography

[1] P. Munk, *A uniform geometrical theory of diffraction for the radiation and mutual coupling associated with antennas on a material coated convex conducting surface.*, PhD thesis, The Ohio-State University Dept. of Electrical Engineering, 1996.

[2] P. E. Hussar and E. M. Smith-Rowland, "An asymptotic solution for boundary-layer fields near a convex impedance surface", *J. of Electromagn. Waves and Appl.*, Vol. 16, no. 2, pp. 185-208, 2002.

[3] G. Hasserjian and A. Ishimaru, "Excitation of a conducting cylindrical surface of large radius of curvature", *IRE Trans. Antennas Propagat.*, Vol.AP-10, pp. 264-273, May 1962.

[4] Z. W. Chang, L. B. Felsen and A. Hessel, "Surface ray methods for mutual coupling in conformal arrays on cylinder and conical surfaces", Polytechnic Institute of New York, Final Rep., prepared under Contract N00123-76-C-0236, 1976.

[5] S. W. Lee and S. Safavi-Naini, "Approximate asymptotic solution of surface field due to a magnetic dipole on a cylinder", *IEEE Trans. Antennas Propagat.*, Vol.AP-26, pp. 593-598, July 1978.

[6] J. Boersma and S. W. Lee, "Surface field due to a magnetic dipole on a cylinder: Asymptotic expansion of exact-solution", Electromagnetics Lab., Dept. of Elec. Eng., Univ. of Illinois, Rep. EM78-17, prepared under Contract N00019-78-C-0064 for Naval Air Systems Command, Dec. 1978.

[7] P. H. Pathak and N. Wang, "Ray analysis of mutual coupling between antennas on a convex surface", *IEEE Trans. Antennas Propagat.*, Vol.AP-29, pp. 911-922, November 1981.

[8] T. S. Bird, "Comparison of asymptotic solutions for the surface field excited by a magnetic dipole on a cylinder", *IEEE Trans. Antennas Propagat.*, Vol.AP-32, pp. 1237-1244, November 1984.

[9] T. S. Bird, "Accurate asymptotic solution for the surface field due to apertures on a cylinder", *IEEE Trans. Antennas Propagat.*, Vol.AP-33, pp. 1108-1117, November 1984.

[10] R. G. Rojas and Z. Al-hekail, "Generalized impedance/resistive boundary conditions for electromagnetic scattering problems", *Radio Sci.*, Vol.24, pp. 1-12, Jan.-Feb. 1989.

[11] R. Paknys and N. Wang, "High -frequency surface field excited by a magnetic line source on an impedance cylinder", *IEEE Trans. Antennas Propagat.*, Vol.35, pp. 293-298, March 1987.

[12] R. J. Pogorzelski, "On the high-frequency asymptotic evaluation of the potentials of elemental sources on an anisotropic impedance cylinder", *Radio Sci.*, Vol.31, pp. 389-399, Mar.-Apr. 1996.

[13] Ç. Tokgöz and R. J. Marhefka, "Surface field excitation by a magnetic point source on an impedance cylinder", *IEEE Antennas and Propagat. Symposium Dig.*, Vol.4, pp. 2834-2837, July 1999.

[14] Ç. Tokgöz, *Asymptotic high frequency analysis of the surface fields of a source excited circular cylinder with an impedance boundary condition.*, PhD thesis, The Ohio-State University Dept. of Electrical Engineering, 2002.

[15] Ç. Tokgöz, P. H. Pathak and R. J. Marhefka, "An asymptotic solution for the surface magnetic field within the paraxial region of a circular cylinder with an impedance boundary condition", *IEEE Trans. Antennas Propagat.*, Vol.53, pp. 1435-1443, April 2005.

[16] V. B. Ertürk and R. G. Rojas, “Efficient computation of surface fields excited on a dielectric coated circular cylinder”, *IEEE Trans. Antennas Propagat.*, Vol.48, pp. 1507-1516, October 2000.

[17] P. Persson and R. G. Rojas, “High frequency approximation for mutual coupling calculations between apertures on a PEC circular cylinder covered with a dielectric layer: non-paraxial region”, *Radio Science*, Vol.38, No.4, pp. 18-1-18-4, July/August 2003.

[18] P. Persson, B. Thors and R. G. Rojas, “An improved numerical approach for surface field calculations on large dielectric coated circular cylinders”, Division of Electromagnetic Theory, Royal Institute of Technology, TRITA-TET 03-4, June 2003.

[19] P. Persson, B. Thors and R. G. Rojas, “An improved algorithm for surface field calculations on large dielectric covered circular cylinders using asymptotic techniques”, 2003 IEEE Int. Antennas Propagation & Symposium and USNC/CNC/URSI Meeting, June 22-27, 2003, Columbus, OH.

[20] R. F. Harrington, *Time-Harmonic Electromagnetic Fields*, McGraw-Hill, New York, 1961.

[21] M. Abramowitz and I. A. Stegun, *Handbook of Mathematical Functions with Formulas, Graphs, and Mathematical Tables*, New York: Dover, 1964.

[22] L. W. Pearson, “A scheme for automatic computation of Fock-type integrals”, *IEEE Trans. Antennas Propagat.*, Vol.35, pp. 1111-1118, October 1987.

[23] N. A. Logan and K. S. Yee, “A simple expression for propagation constants associated with a reactive convex surface”, *IRE Trans. Antennas Propagat.*, Vol. Ap-10, pp. 103, Jan. 1962.

[24] D. A. Hill and J. R. Wait, “Ground wave attenuation function for a spherical earth with arbitrary surface impedance”, *Radio Sci.*, Vol.15, pp. 637-643, May-June 1980.

[25] L. B. Felsen and K. Naishadham, "Ray formulation of waves guided by circular cylindrical stratified dielectrics", *Radio Sci.*, Vol.26, pp. 203-209, January-February 1991.

[26] J. B. Keller, S. I. Rubinow and M. Goldstein, "Zeros of Hankel functions and poles of scattering amplitudes", *Journal of Mathematical Physics*, Vol.4, No. 6, pp. 829-832, June 1963.

[27] W. C. Chew, *Waves and Fields in Inhomogeneous Media*, Van Nostrand Reinhold, 1990.

[28] R. E. Collin, *Field Theory of Guided Waves*, McGraw-Hill, New York, 1960.